Monthly Notices
of the
ROYAL ASTRONOMICAL SOCIETY

MNRAS **491,** 5925–5950 (2020) doi:10.1093/mnras/stz3441

Spectral library of age-benchmark low-mass stars and brown dwarfs

E. Manjavacas [1,2★] N. Lodieu,[3,4] V. J. S. Béjar,[3,4] M. R. Zapatero-Osorio,[5] S. Boudreault[6] and M. Bonnefoy[7]

[1] *W. M. Keck Observatory, 65-1120 Mamalahoa Highway, Kamuela, HI 96743, USA*
[2] *Department of Astronomy/Steward Observatory, The University of Arizona, 933 N. Cherry Avenue, Tucson, AZ 85721, USA*
[3] *Instituto de Astrofísica de Canarias, C/ Vía Láctea s/n, E38205 La Laguna, Tenerife, Spain*
[4] *Departamento de Astrofísica, Universidad de La Laguna, Avda. Astrofísico Francisco Sánchez s/n, 38206 La Laguna, Tenerife, Spain*
[5] *Centro de Astrobiología (CSIC-INTA), Crta. Ajalvir km 4, E-28850 Torrejón de Ardoz, Madrid, Spain*
[6] *Max-Planck-Institut für Sonnensystemforschung, Justus-von-Liebig-Weg 3, 37077 Göttingen, Germany*
[7] *Université Grenoble Alpes, CNRS, IPAG, 38000 Grenoble, France*

Accepted 2019 December 5. Received 2019 December 4; in original form 2019 August 29

ABSTRACT

In recent years, some extremely red brown dwarfs have been discovered. They were believed to have a low surface gravity, but many of their spectral characteristics are similar to those of high-surface-gravity brown dwarfs, showing that the spectral characteristics of young brown dwarfs are poorly understood. We aim to test surface-gravity indicators in late-M and early-L brown dwarf spectra using data obtained with the X-shooter spectrograph at the Very Large Telescope. We select a benchmark sample of brown dwarf members of Chamaeleon I (∼2 Myr), Upper Scorpius (5−10 Myr), the Pleiades (132 ± 27 Myr) and Praesepe (590−790 Myr) with well-constrained ages and similar metallicities. We provide a consistent spectral classification of the sample in the optical and in the near-infrared. We measure the equivalent widths of their alkali lines, finding that they have a moderate correlation with age, especially for objects with spectral types M8 and later. We use spectral indices defined in the literature to estimate surface gravity, finding that their gravity assignment is accurate for 75 per cent of our sample. We investigate the correlation between red colour and age, finding that after ∼10 Myr, the colour does not change significantly for our sample with spectral types M6.0–L3.0. In this case, the red colours might be associated with circumstellar discs, ring structures, extinction, or viewing angle. Finally, we calculate the bolometric luminosity, and *J* and *K* bolometric corrections for our sample. We find that six objects are overluminous compared with other members of the same association. These objects are flagged as binary candidates by the *Gaia* survey.

Key words: brown dwarfs – stars: fundamental parameters.

1 INTRODUCTION

Brown dwarfs are substellar objects that are unable to sustain hydrogen fusion. From their birth, brown dwarfs cool down with time and contract. During this process, they change spectral type, through M, L, T and Y, changing their luminosity and chemistry (Kirkpatrick et al. 2012). As a result of this evolution, the spectral type does not constrain the substellar mass, and we need ages to estimate masses using evolutionary models for substellar objects (Burrows et al. 1997; Baraffe et al. 2015).

Brown dwarfs contract as they cool down over their lifetime, and therefore younger brown dwarfs (<100 Myr) have larger radii and lower gravity ($g = GM/R^2$) than their older counterparts in the field (>500 Myr). Young brown dwarfs and exoplanet atmospheres are expected to share similar colours, temperatures and surface gravities (Chauvin et al. 2004; Marois et al. 2008; Faherty et al. 2013). However, young brown dwarfs, unlike exoplanets, are isolated and not close to their parent star, which make them easier to observe, especially for spectroscopic studies. The study of young free-floating brown dwarfs are excellent proxies to improve our understanding of the atmospheres of imaged young giant exoplanets.

Gravity affects brown dwarf atmospheres, changing their spectral characteristics. Many atomic lines and molecular bands are weaker in the spectra of young brown dwarfs than in their higher-gravity counterparts. The neutral alkali lines are weaker over the whole optical and near-infrared spectrum: Rb I at 794.8 nm, Na I at 818.3 nm, Na I at 819.5 nm, Cs I at 852.0 nm, K I at 1169 nm, K I

★ E-mail: elenamanjavacas@gmail.com

at 1177 nm, K I at 1243 nm and K I at 1253 nm (Martín, Rebolo & Zapatero-Osorio 1996; Gorlova et al. 2003; McGovern et al. 2004; Martín et al. 2017, and references therein; see Schlieder et al. 2012 for a theoretical explanation). In addition, FeH absorptions in the *J* and *H* bands are also less prominent for low-gravity dwarfs (Allers & Liu 2013; Lodieu et al. 2018, among others). In contrast, the VO bands at 0.74, 0.96, 1.06 and 1.18 μm, and the TiO bands at 0.71, 0.76, 0.82, 0.84 and 1.25 μm are stronger for low-surface-gravity objects (Martín, Rebolo & Zapatero-Osorio 1996; Zapatero Osorio, Rebolo & Martin 1997; Allers & Liu 2013, and references therein), particularly in L dwarfs (Allers & Liu 2013), owing to inefficient condensation (Lodders 2002). In addition, very red colours were also believed to be an indication of low surface gravity, because low surface gravity was expected to prevent the settling of the dust in the upper atmosphere. In recent years, several tens of very red L brown dwarfs (Kirkpatrick et al. 2006; Stephens et al. 2009; Gizis et al. 2012; Liu et al. 2013; Marocco et al. 2014; Filippazzo et al. 2015; Faherty et al. 2016; Liu et al. 2016; Schneider et al. 2014, 2017; Best et al. 2017, among others) have been found in large surveys, such as 2MASS (Two Micron All Sky Survey, Skrutskie et al. 2006), SDSS (Sloan Digital Sky Survey, Blanton et al. 2017) and PanStarrs (Panoramic Survey Telescope and Rapid Response System, Chambers et al. 2016). These very red brown dwarfs were believed to be young; however, some objects did not exhibit clear spectroscopic signposts of low-gravity atmospheres in their spectra, such as, for example, weak alkali lines. This is the case for ULAS J222711 − 004547 (Marocco et al. 2014), 2MASS J035523.37 + 113343.7 (Faherty et al. 2013) and WISEP J004701.06 + 680352.1 (Gizis et al. 2015), among others. These examples suggest that red colours *alone* cannot be used as a signature of youth.

In this paper, we aim to test the most common methods to estimate surface gravity (i.e. age) in brown dwarfs. To achieve this aim, we targeted the spectra of members of open clusters and associations with well-determined ages. We selected 20 members of the Chamaeleon I (Cha I) region (∼2 Myr, Luhman 2007), the Upper Scorpius (UppSco) association (5–10 Myr, Slesnick, Hillenbrand & Carpenter 2008; Song, Zuckerman & Bessell 2012; Feiden 2016; Pecaut & Mamajek 2016; Rizzuto et al. 2016; Fang, Herczeg & Rizzuto 2017), the Pleiades open cluster (132 ± 27 Myr, Stauffer, Schultz & Kirkpatrick 1998; Barrado y Navascués 2004; Dahm 2015; Lodieu et al. 2019) and the Praesepe open cluster (590−790 Myr, Fossati et al. 2008; Delorme et al. 2011; Brandt & Huang 2015; Gossage et al. 2018). The ages of these associations or open clusters correspond respectively to the gravities that define the γ, β and α for low-, intermediate- and field-gravity classification of M and L dwarfs (Cruz, Kirkpatrick & Burgasser 2009), or the VL-G (very low gravity), INT-G (intermediate gravity) and FLD-G (field gravity) classes defined by Allers & Liu (2013).

In Section 2, we describe the selected sample of objects presented in this paper. In Section 3, we provide details of the X-shooter observations and data reduction. In Section 4, we explain the analysis carried out and our results. In Section 5, we derive the physical parameters for our sample using evolutionary models for substellar objects. Finally, in Section 6 we summarize our results.

2 SAMPLE SELECTION

We selected a sample of 20 benchmark objects with confirmed membership of open clusters or associations, with known ages, metallicities and distances. We chose a sample with photometry and optical spectral types confirming membership. In the case of the Pleiades and Praesepe, members are confirmed not only by photometry and optical spectroscopy, but also by proper motion (Lodieu, Deacon & Hambly 2012b; Boudreault et al. 2012; Bouy et al. 2015). We selected objects in each of the associations or open clusters with magnitude ranging from $J = 14.9$ to $J = 18.1$ mag, which allowed us to obtain spectroscopy with a signal-to-noise ratio of between 4 and 53 in the near-infrared, using exposure times of between 40 min and 1.5 h. Our sample has spectral types between M5.5 and L3.5, with at least one target per open cluster or association of each spectral type between M5.5 and L0. To complete our sample in age range, we added three members from the UppSco association, and four from the Cha I region from proposals: 093.C-0109(A) (P.I. Van der Plas), 093.C-0769(A) (P.I. Bonnefoy) and 095.C-0378(A) (P.I. Testi). We list the objects in our sample with their main characteristics in Table 1.

We selected four members of the Cha I region (Prusti et al. 1991; Boulanger et al. 1998; Mamajek, Lawson & Feigelson 2000; Winston et al. 2012, and references therein). Cha I is a molecular cloud with ongoing star formation owing to its young age (∼2 Myr Luhman 2007), but is old enough to have relatively low extinction ($A_V \leq 5$ mag). Roccatagliata et al. (2018) found that Cha I has a double population, one north and one south, with slightly different distances. The northern one is at 192.7 ± 0.4 pc, while the southern one is at 186.5 ± 0.7 pc, with nearly solar metallicity ([Fe/H] = − 0.08 ± 0.04 dex; Spina et al. 2014). All our Cha I targets lie in the northern cloud, with the exception of 2MASS J11123099 − 765334.

We have three members in our sample that belong to the UppSco association. UppSco (de Zeeuw et al. 1999; Kraus et al. 2008; Pecaut, Mamajek & Bubar 2012; Lodieu 2013, and references therein) is part of the Scorpius Centaurus association, with an estimated age of 5–10 Myr (Slesnick et al. 2008; Song et al. 2012; Feiden 2016; Pecaut & Mamajek 2016; Rizzuto et al. 2016; Fang et al. 2017), and nearly solar metallicity ([Fe/H] = 0.02 dex, Carpenter, Ricci & Isella 2014). Its recent average updated distance from *Gaia* is $d = 144 \pm 2$ pc, with a standard deviation of ±17.2 pc (Fang et al. 2017).

Seven objects of our sample are members of the Pleiades open cluster. The Pleiades (Zapatero Osorio et al. 1997; Bouvier et al. 1998; Moraux et al. 2003; Deacon & Hambly 2004; Lodieu et al. 2012a, and references therein) is an intermediate-age open cluster (132 ± 27 Myr, according to the most recent estimate from Lodieu et al. 2019), with solar metallicity (Soderblom et al. 2009) at a distance of 139.41 ± 0.08 pc (Gaia Collaboration et al. 2018), although more recently Lodieu et al. (2019) provided a distance of 135.15 ± 0.43 pc. The cluster has low foreground extinction, $E(B - V) = 0.04$ mag, as determined by Breger (1986).

Finally, six of the members of our sample belong to the Praesepe open cluster (Jones & Stauffer 1991; Pinfield et al. 2003; Boudreault et al. 2012; Brandt & Huang 2015, and references therein). The Praesepe is the oldest cluster of our sample, with an age between 590 and 790 Myr, (Fossati et al. 2008; Delorme et al. 2011; Brandt & Huang 2015; Gossage et al. 2018; Martín et al. 2018), and a metallicity of [Fe/H] = 0.12–0.16 dex (Netopil et al. 2016). Its most updated distance provided by *Gaia* (Gaia Collaboration et al. 2018; Lodieu et al. 2019) is 186.18 ± 0.11 pc. The Praesepe has a low reddening along the line of sight of $E(B - V) = 0.027 \pm 0.04$ (Taylor 2006).

Table 1. List of observed targets with their full name, coordinates, magnitude, spectral types, cluster or association membership, and flag for disc-bearing sources and binary candidates.

Num.	Name	RA	Dec.	J [mag]	Opt. sp. type	NIR sp. type	Open cluster/association	Disc?	Binary candidate?	Ref.
1	UGCS J083748.00 + 201448.5	08 37 48.01	+20 14 48.6	16.50 ± 0.01			Praesepe (590 − 790 Myr)	NR[a]	NR[b]	1
2	2MASS J08370215 + 1952074	08 37 02.13	+19 52 07.4	15.69 ± 0.01	M7 [29]		Praesepe (590 − 790 Myr)	NR[a]	Yes	2, 31
3	UGCS J083654.60 + 195415.7	08 36 54.60	+19 54 15.7	17.11 ± 0.02			Praesepe (590 − 790 Myr)	NR[a]	NR[b]	2
4	2MASS J08410852 + 1954018	08 41 08.54	+19 54 01.0	16.45 ± 0.01			Praesepe (590 − 790 Myr)	NR[a]	Yes	2, 31
5	2MASS J08370450 + 2016033	08 37 04.49	+20 16 03.2	16.82 ± 0.02			Praesepe (590 − 790 Myr)	NR[a]	Yes	3, 31
6	UGCS J084510.65 + 214817.0	08 45 10.66	+21 48 17.1	17.42 ± 0.03	L0.5 [28]		Praesepe (590 − 790 Myr)	NR[a]	Yes	3, 31
7	2MASS J03484469 + 2437236	03 48 44.69	+24 37 23.6	14.90 ± 0.01		M5.5 [25]	Pleiades (132 ± 27 Myr)	NR[a]	Yes	4, 31
8	2MASS J03491512 + 2436225	03 49 15.12	+24 36 22.5	15.17 ± 0.01	M6.5 [27]	M6.5 [25]	Pleiades (132 ± 27 Myr)	NR[a]	NR[b]	5
9	2MASS J03512557 + 2345214	03 51 25.57	+23 45 21.4	16.13 ± 0.03	M8.0 [26]	M8.0 [25]	Pleiades (132 ± 27 Myr)	NR[a]	NR[b]	6
10	2MASS J03443516 + 2513429	03 44 35.16	+25 13 42.9	15.66 ± 0.01		M9.3 [25]	Pleiades (132 ± 27 Myr)	NR[a]	Yes	7, 31
11	2MASS J03463425 + 2350036	03 46 34.25	+23 50 03.6	17.46 ± 0.03			Pleiades (132 ± 27 Myr)	NR[a]	NR[b]	8
12	2MASS J03461406 + 2321565	03 46 14.06	+23 21 56.5	15.67 ± 0.02			Pleiades (132 ± 27 Myr)	NR[a]	NR[b]	9
13	2MASS J03541027 + 2341402	03 54 10.27	+23 41 40.2	18.14 ± 0.05		L3.0 [25]	Pleiades (132 ± 27 Myr)	NR[a]	NR[b]	10
14	2MASS J15591135 – 2338002	15 59 11.35	–23 38 00.2	14.40 ± 0.04	M7.0 [11]		UppSco (5–10 Myr)	Yes	NR[b]	11, 17
15	2MASS J16060391 – 2056443	16 06 03.91	–20 56 44.3	13.53 ± 0.03	M7.0 [24]		UppSco (5–10 Myr)	Yes	NR[b]	12, 18
16	2MASS J16060629 – 2335133	16 06 06.29	–23 35 13.3	16.23 ± 0.01	M9 [23]	L0.0 [13]	UppSco (5–10 Myr)	NR[a]	NR[b]	13
17	2MASS J11085497 – 7632410	11 08 54.97	–76 32 41.0	13.06 ± 0.03	M5.5 [22]		Cha I (∼2 Myr)	Yes	NR[b]	14, 19
18	2MASS J11123099 – 7653342	11 12 30.99	–76 53 34.2	14.07 ± 0.03	M7.0 [21]	M7.0 [21]	Cha I (∼2 Myr)	NR[a]	NR[b]	15
19	2MASS J11074656 – 7615174	11 07 46.56	–76 15 17.4	13.94 ± 0.03	M6.5 [30]		Cha I (∼2 Myr)	Yes	NR[b]	30
20	2MASS J11062554 – 7633418	11 06 25.54	–76 33 41.8	13.00 ± 0.03	M5.5 [30]		Cha I (∼2 Myr)	Yes	NR[b]	30

Notes. References: [1] Boudreault et al. (2010), [2] Hodgkin et al. (1999), [3] Boudreault et al. (2012), [4] Bouvier et al. (1998), [5] Stauffer et al. (1998), [6] Bouvier et al. (1998), [7] Bouvier et al. (1998), [8] Nagashima et al. (2003), [9] Lodieu, Deacon & Hambly (2012a), [10] Bihain et al. (2006), [11] Ardila, Martín & Basri (2000), [12] Martín, Delfosse & Guieu (2004), [13] Lodieu et al. (2007), [14] Persi et al. (2000), [15] López Martí et al. (2004).

References of disks detections: [16] Luhman & Muench (2008), [17] van der Plas et al. (2016), [18] Herczeg et al. (2009), [19] Long et al. (2017).

[a]NR: the existence of a disc has not been reported for this object.

References for spectral type: [20] Alves de Oliveira et al. (2012), [21] Luhman (2007), [22] Luhman (2004), [23] Lodieu et al. (2018), [24] Slesnick et al. (2008), [25] Bihain et al. (2010), [26] Martín et al. (1996), [27] Stauffer et al. (1998), [28] Boudreault & Lodieu (2013), [29] West et al. (2011), [30] Manara et al. (2017).

References for binary candidates: [31] Gaia Collaboration et al. (2018).

[b]NR: not reported as a binary candidate in the literature.

Table 2. List of derived optical and near-infrared spectral types using field and young brown dwarfs.

Num.	Name	Opt. sp. type, field	Opt. sp. type, young	NIR sp. type, field	NIR sp. type, young
1	UGCS J083748.00 + 201448.5	M7.0	M5.5	M6.0	M8.0
2	2MASS J08370215 + 1952074	M6.0	M7.0	M7.5	M8.0
3	UGCS J083654.60 + 195415.7	M8.0	M7.25	M7.0	M8.0
4	2MASS J08410852 + 1954018	M8.0	M8.0	M9.0	M8.0
5	2MASS J08370450 + 2016033	L0.0	L1.0	L0.0	L0.0
6	UGCS J084510.65 + 214817.0	L1.5	L1.0	L1.5	L2.0
7	2MASS J03484469 + 2437236	M6.0	M5.5	M6.0	M6.0
8	2MASS J03491512 + 2436225	M7.0	M6.5	M6.0	M6.0
9	2MASS J03512557 + 2345214	M6.5	M6.5	M7.0	M7.25
10	2MASS J03443516 + 2513429	M7.5	M6.5	M7.0	M7.0
11	2MASS J03463425 + 2350036	L0.0	L1.0	L1.0	L2.0
12	2MASS J03461406 + 2321565	M7.0	M6.5	M7.0	M6.0
13	2MASS J03541027 + 2341402	NA	NA	L3.0	L3.0
14	2MASS J15591135 – 2338002	M7.5	M7.0	M8.5	M7.25
15	2MASS J16060391 – 2056443	M8.0	M7.5	M8.5	M7.0
16	2MASS J16060629 – 2335133	L0.0	L1.0	M9.5	M9.0
17	2MASS J11085497 – 7632410	M7.0	M6.0	M8.0	M6.0
18	2MASS J11123099 – 7653342	M7.0	M6.5	M7.0	M7.0
19	2MASS J11074656 – 7615174	M7.0	M6.5	M8.0	M8.0
20	2MASS J11062554 – 7633418	M6.0	M5.75	M8.0	M6.0

Note. NA: spectrum not available.

Table 3. List of measured lines in the optical spectra with the central wavelength of the line and continuum edges.

Line	λ_{line} [nm]	Continuum 1 [nm]	Continuum 2 [nm]
Li I	670.8	669.0	672.0
Hα	656.3	655.0	657.0
Rb I	794.8	792.7	797.5
Na I	818.3	817.7	818.8
Na I	819.5	819.0	819.5
Cs I	852.0	851.0	853.4

3 OBSERVATIONS AND DATA REDUCTION

Our targets were observed between 2016 October and 2017 January, under proposal number ID: 098.C-0277(A) (P.I. Manjavacas), using the X-shooter spectrograph (Vernet et al. 2011), mounted on the Kueyen (UT2,VLT) telescope at Paranal Observatory. X-shooter is composed of three arms: UVB (300–550 nm), optical (550–1000 nm) and near-infrared (1000–2500 nm). It was operated in echelle slit nod mode, using the 1.3-arcsec slit width for the UVB arm, and the 1.2-arcsec slit width for the optical and the near-infrared arms. This setup provides resolutions of ∼2030 in the UVB, ∼3360 in the VIS, and ∼3900 in the near-infrared. The average signal-to-noise ratio of each spectra in the optical and near-infrared is shown in Table A1 of the Appendix. Observations were performed at the parallactic angle to mitigate the effect of differential chromatic refraction. We moved the object along the slit between two positions following an ABBA pattern with a size of 6 arcsec. The flux expected in the UVB arm is extremely low, and therefore we chose not to use spectra taken in this range. Telluric standards were observed before or after every target at similar airmass. Bias, darks and flats were taken every night. Arc frames were taken every second day. The observing log, including telluric standard stars and the raw seeing during the observations, is shown in Table A1 of the Appendix.

The spectra were reduced using the ESO X-shooter pipeline version 1.3.7. In the reduction cascade, the pipeline deletes the non-linear pixels and subtracts bias in the optical or dark frames in the near-infrared. It generates a guess order from a format-check frame, a reference list of arc line, and a reference spectral format table. It refines the guess-order table by illuminating the instrument pinhole with a continuum lamp. A master flat frame and the order tables tracing the flat edges are created. Finally, the pipeline determines the instrumental response.

In the case of the near-infrared, we extracted the 2D spectrum provided by the pipeline with the `APALL` routine in IRAF (Image Reduction and Analysis Facility, Tody 1986, 1993).[1] We used the spectrum of the telluric calibration star of the corresponding science target observed on the same night to correct for instrumental response and to remove telluric lines. First, we removed artefacts and cosmic rays from the calibration stars. We also removed the H and He absorption lines from their spectra using a Legendre polynomial fit of the pseudo-continuum around the line. We then derived a response function by dividing the non-flux-calibrated clean spectrum of the calibration standard by a blackbody synthetic spectrum with the same temperature as the telluric star (Theodossiou & Danezis 1991). Finally, we divided our spectra by the corresponding response function calculated with the spectrum of the respective calibration star, eliminating the telluric absorption bands and correcting for the instrumental response simultaneously.

We flux-calibrated our near-infrared spectra using the *J*-band magnitudes given by 2MASS (Skrutskie et al. 2006) or UKIDSS (UKIRT Infrared Deep Sky Survey; Lawrence et al. 2007) for our targets. We convolved our near-infrared spectra with the *J*-filter transmission curves of 2MASS or UKIDSS, depending on the object. The convolved spectra were integrated over the *J*-band wavelength range, and the results were taken to the observed

[1]IRAF is distributed by the National Optical Astronomy Observatory, which is operated by the Association of Universities for Research in Astronomy (AURA) under a cooperative agreement with the National Science Foundation.

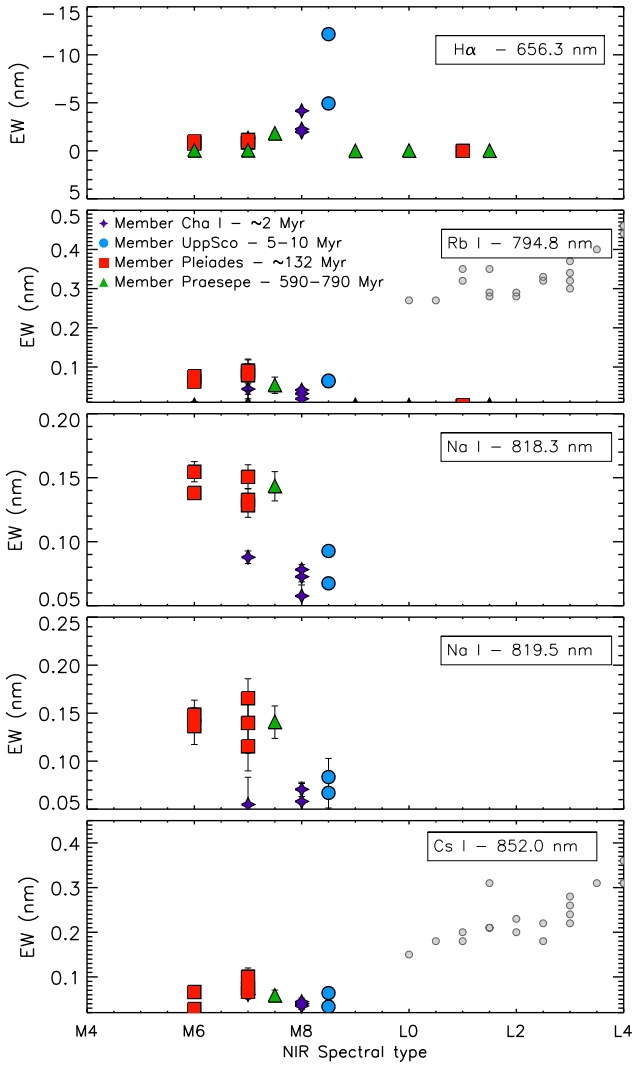

Figure 1. Equivalent widths of the detected alkali lines and of the Hα line in the optical for our benchmark objects with different ages: purple crosses, blue circles, red squares and green triangles. Grey circles represent other L dwarfs from Chiu et al. (2006), Golimowski et al (2004) and Knapp et al. (2004).

photometric fluxes. This procedure is affected by the error bars of the *J*-band magnitudes and the uncertainties introduced during the response correction.

To flux-calibrate the optical X-shooter spectra, we calculated a scaling factor in the overlapping wavelengths of the optical and near-infrared spectra (995−1020 nm), to match the optical and the near-infrared data.

In addition, we carried out low-resolution optical spectroscopy with the Optical System for Imaging and low Resolution Integrated Spectroscopy (OSIRIS; Cepa, Bland-Hawthorn & González 2000) mounted on the 10.4-m Gran Telescopio Canarias (GTC) in the Roque de Los Muchachos Observatory in La Palma (Canary Islands) under programme GTC66-12B (P.I. Boudreault). We used the R300R grism and a 1.0-arcsec slit with a 2 × 2 binning of the detector, yielding a spectral resolution of ∼300 at 680 Å. This configuration shows contamination from the second-order light redwards of 9000 Å. Therefore, we restricted the range of analysis of our spectra to the 5500–9000 Å wavelength range. We observed six members of Praesepe and one member of the Pleiades (see Table A2 in the Appendix for a log of observations) under grey time, spectroscopic conditions, and seeing better than 1.2 arcsec. We offset the object along the slit in case of for several exposures. We reduced the optical spectra using standard IRAF packages (Tody 1986, 1993). To summarize, we first subtracted the overscan and removed the flat-field contribution before trimming the images with the `ccdred` package. Then we optimally extracted the spectrum that we calibrated in wavelength using a combination of HgAr, Ne and Xe lamps. To flux-calibrate GTC/OSIRIS optical spectra, we followed a similar procedure for the near-infrared data, but we used the Pan-STARRS (Panoramic Survey Telescope and Rapid Response System; Chambers et al. 2016) *i* filter. The final X-shooter and OSIRIS spectra are presented in Figs A1, A2, A3 and A4 of the Appendix.

4 ANALYSIS AND RESULTS

4.1 Spectral types

We aimed at performing a consistent spectral classification of the objects in our sample in the optical and in the near-infrared independently. Within both wavelength ranges, we performed two classifications: one comparing our spectra with field late M- and early L-type dwarfs published in different spectral libraries, and a second comparing our sample with young brown dwarf spectra of the same types. For this purpose, we compared our optical spectra with optical young spectral libraries (Luhman & Mamajek 2010; Luhman et al. 2018; Lodieu et al. 2018), and field brown dwarf spectral libraries (Kirkpatrick et al. 1999), determining the best match to both young and field optical spectra. For the comparison, we degraded the resolution of our X-shooter spectra to the resolution of the corresponding comparison spectra. To determine the best match for each object and wavelength range, we used the following expression as in Cushing et al. (2008):

$$G = \sum_{\lambda} \left[\frac{C(\lambda) - \alpha T(\lambda)}{\sigma_c(\lambda)} \right]^2, \quad (1)$$

where $C(\lambda)$ is the spectrum of our object, $T(\lambda)$ is the comparison spectrum, α is a scaling factor that minimizes G, and $\sigma_c(\lambda)$ are the uncertainties of the target spectrum. In Table 2 we summarize the optical and near-infrared spectral types obtained from the best matches. We show the best matches for Praesepe, the Pleiades, USco, and Cha in Figs 1 and 2, 3 and 4, 5 and 6, and 7 and 8, respectively.

We find a maximum dispersion of ±2.5 spectral types between the different spectral classifications, for members of the Praesepe, and for members of the Chamaelon I association. Differences in spectral classification using different wavelengths and type of objects are expected, as the spectral characteristics of brown dwarfs and low-mass stars evolve with age (i.e. surface gravity). This probably explains why fitting field brown dwarf spectra to younger brown dwarf spectra and vice versa might provide slightly different spectral types.

In addition, we need to highlight that the three Cha I members (2MASS J11062554 – 76334, 2MASS J11074656 – 76151 and 2MASS J11085497 – 763241) and two UppSco members (2MASS J15591135 – 233800 and 2MASS J16060391 – 20564) harbour discs (see Table 1 for details). As a consequence, their spectral energy distributions (SEDs) usually show near- or mid-infrared excesses, which might lead to later spectral type estimates.

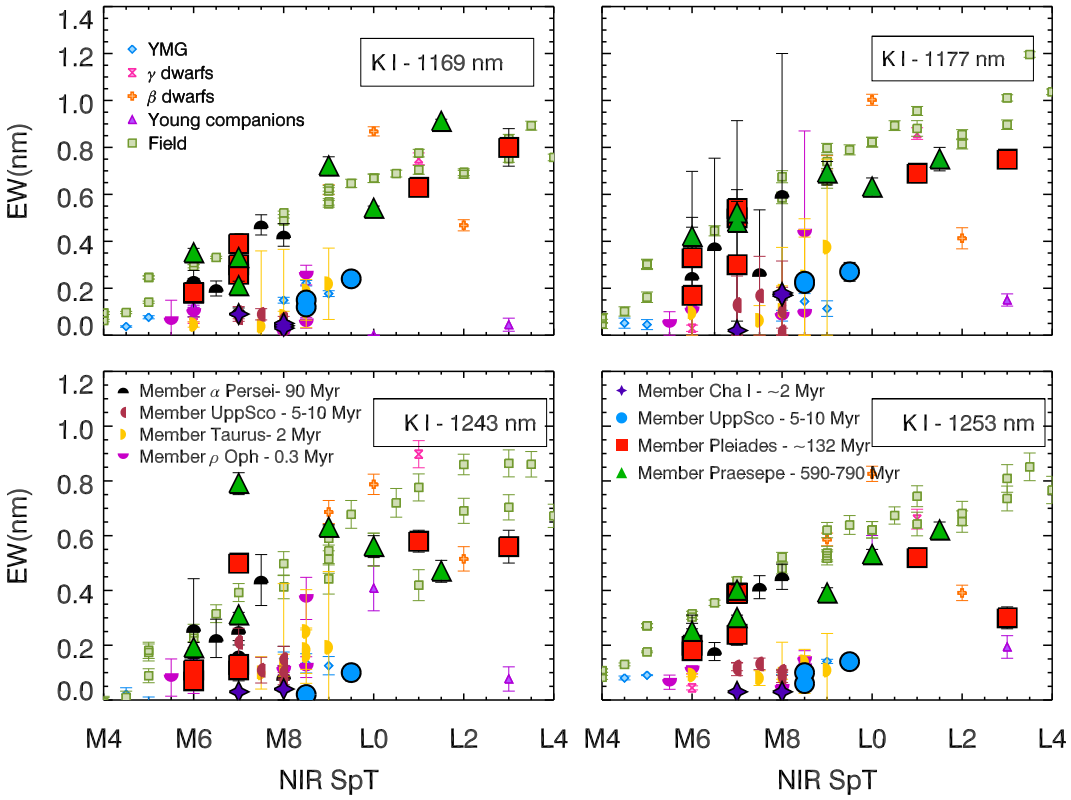

Figure 2. Equivalent widths of the detected alkali lines in the near-infrared for our benchmark objects with different ages: purple crosses, blue circles, red squares, and green triangles. We overplot field objects (McLean et al. 2003; Cushing et al. 2005), objects that belong to the TW Hydrae Association (TWA), young companions (Allers & Liu 2013; Bonnefoy et al. 2014b), and young β dwarfs and γ dwarfs as a comparison (Allers & Liu 2013). We include the pEWs published by Martín et al. (2017) of confirmed members of α Persei (90 Myr, black half-upper circle), of UppSco (5–10 Myr, red half-left circles), of Taurus (2 Myr, yellow half-right circles), and of ρ Ophiuchi (0.3 Myr, pink half-down circles).

Table 4. Equivalent widths in nanometres for alkali lines, and Hα emission measured in the optical. Negative values indicate lines in emission.

Name	NIR sp. type	Hα [1]	He I [2]	Li I [3]	Rb I [4]	Na I [5]	Na I [6]	Cs I [7]
UGCS J083748.00 + 201448.5	M7.0	<0.02	NA	NA	<0.01	NA	NA	NA
2MASS J08370215 + 1952074	M8.0	−1.79 ± 0.20	<0.14	<0.15	0.05 ± 0.02	0.14 ± 0.01	0.15 ± 0.01	0.06 ± 0.01
UGCS J083654.60 + 195415.7	M8.0	<0.02	NA	NA	<0.02	NA	NA	NA
2MASS J08410852 + 1954018	M9.0	<0.02	NA	NA	NA	NA	NA	NA
2MASS J08370450 + 2016033	L0.0	NA	NA	NA	NA	NA	NA	NA
UGCS J084510.65 + 214817.0	L1.5	NA	NA	NA	NA	NA	NA	NA
2MASS J03484469 + 2437236	M6.0	−0.75 ± 0.05	NA	<0.04	0.06 ± 0.10	0.15 ± 0.01	0.14 ± 0.01	0.03 ± 0.01
2MASS J03491512 + 2436225	M6.0	−0.97 ± 0.06	NA	<0.06	0.07 ± 0.01	0.14 ± 0.01	0.14 ± 0.01	0.07 ± 0.01
2MASS J03512557 + 2345214	M7.0	−1.14 ± 0.32	<0.14	<0.58	0.09 ± 0.03	0.15 ± 0.01	0.16 ± 0.02	0.07 ± 0.02
2MASS J03443516 + 2513429	M8.5	−0.87 ± 0.41	−0.37 ± 0.27	<0.38	0.08 ± 0.04	0.13 ± 0.01	0.12 ± 0.02	0.10 ± 0.02
2MASS J03463425 + 2350036	L1.0	NA	NA	NA	NA	NA	NA	NA
2MASS J03461406 + 2321565	M7.0	−0.89 ± 0.19	−0.09 ± 0.15	<0.14	0.09 ± 0.02	0.13 ± 0.01	0.17 ± 0.01	0.07 ± 0.01
2MASS J03541027 + 2341402	L3.0	NA	NA	NA	NA	NA	NA	NA
2MASS J15591135 – 2338002	M8.5	−4.93 ± 0.03	−0.17 ± 0.03	0.04 ± 0.01	0.06 ± 0.01	0.09 ± 0.01	0.08 ± 0.01	0.06 ± 0.01
2MASS J16060391 – 2056443	M8.5	−12.15 ± 0.07	−0.09 ± 0.01	0.02 ± 0.01	0.06 ± 0.01	0.07 ± 0.01	0.07 ± 0.01	0.03 ± 0.01
2MASS J16060629 – 2335133	M9.5	−2.16 ± 0.30	<0.02	0.35 ± 0.10	0.13 ± 0.06	0.12 ± 0.01	0.13 ± 0.02	0.09 ± 0.04
2MASS J11085497 – 7632410	M6.0	−4.16 ± 0.01	−0.024 ± 0.10	<0.01	<0.02	0.06 ± 0.01	0.07 ± 0.01	0.04 ± 0.01
2MASS J11123099 – 7653342	M7.0	−1.32 ± 0.08	−0.15 ± 0.06	<0.07	0.04 ± 0.01	0.09 ± 0.01	0.05 ± 0.02	0.06 ± 0.01
2MASS J11074656 – 7615174	M8.0	−2.26 ± 0.03	<0.02	0.05 ± 0.02	0.04 ± 0.01	0.08 ± 0.01	0.06 ± 0.01	0.03 ± 0.01
2MASS J11062554 – 7633418	M8.0	−1.96 ± 0.01	NA	0.04 ± 0.01	0.03 ± 0.01	0.07 ± 0.01	0.03 ± 0.01	0.04 ± 0.01

Note. Line wavelengths: [1] Hα, 656.3 nm; [2] He I, 667.7 nm; [3] Li I, 670.8 nm; [4] Rb I, 794.8 nm; [5] Na I, 818.3 nm; [6] Na I, 819.5 nm; [7] Cs I, 852.0 nm.

For the subsequent analysis in this paper, we will adopt as the final spectral classification the one provided by the comparison with near-infrared field objects (third column in Table 2). The reason for the choice of this spectral classification is that most of the flux of the objects in our sample is in this wavelength range. The reason we chose field objects for the spectral classification is that they provide a reasonable fit for most of the object's near-infrared spectra. In addition, the spectral classification sequence of field low-mass stars

Table 5. Equivalent widths in nanometres for alkali lines measured in the near-infrared.

Name	NIR sp. type	K I (1169 nm)	K I (1177 nm)	K I (1243 nm)	K I (1253 nm)	GS[a,b]	OC/A[c]
UGCS J083748.00 +201448.5	M6.0	0.35 ± 0.02	0.42 ± 0.04	0.19 ± 0.02	0.25 ± 0.01	00–0 / FLD-G	Praesepe
2MASS J08370215 + 1952074	M7.5	0.21 ± 0.02	0.48 ± 0.03	0.31 ± 0.01	0.30 ± 0.01	11–1 / INT-G	Praesepe
UGCS J083654.60 + 195415.7	M7.0	0.33 ± 0.01	0.52 ± 0.05	0.79 ± 0.04	0.40 ± 0.02	11–1 / INT-G	Praesepe
2MASS J08410852 + 1954018	M9.0	0.72 ± 0.04	0.69 ± 0.05	0.63 ± 0.01	0.39 ± 0.02	01–1 / FLD-G	Praesepe
2MASS J08370450 + 2016033	L0.0	0.54 ± 0.01	0.63 ± 0.04	0.56 ± 0.04	0.53 ± 0.02	11–1 / INT-G	Praesepe
UGCS J084510.65 + 214817.0	L1.5	0.91 ± 0.01	0.75 ± 0.05	0.47 ± 0.04	0.62 ± 0.03	01–1 / FLD-G	Praesepe
2MASS J03484469 + 2437236	M6.0	0.18 ± 0.01	0.17 ± 0.03	0.07 ± 0.02	0.18 ± 0.01	02–1 / INT-G	Pleiades
2MASS J03491512 + 2436225	M6.0	0.18 ± 0.01	0.33 ± 0.02	0.11 ± 0.02	0.20 ± 0.01	00–1 / FLD-G	Pleiades
2MASS J03512557 + 2345214	M7.0	0.30 ± 0.01	0.50 ± 0.03	0.11 ± 0.04	0.39 ± 0.02	00–0 / FLD-G	Pleiades
2MASS J03443516 + 2513429	M7.0	0.39 ± 0.01	0.54 ± 0.04	0.50 ± 0.02	0.39 ± 0.01	00–0 / FLD-G	Pleiades
2MASS J03463425 + 2350036	L1.0	0.63 ± 0.01	0.69 ± 0.04	0.58 ± 0.04	0.52 ± 0.03	11–1 / INT-G	Pleiades
2MASS J03461406 + 2321565	M7.0	0.26 ± 0.01	0.30 ± 0.02	0.13 ± 0.02	0.24 ± 0.01	12–1 / INT-G	Pleiades
2MASS J03541027 + 2341402	L3.0	0.80 ± 0.08	0.75 ± 0.02	0.56 ± 0.06	0.30 ± 0.04	11–2 / INT-G	Pleiades
2MASS J15591135 – 2338002	M8.5	0.15 ± 0.02	0.23 ± 0.02	<0.02	0.10 ± 0.01	22–2 / VL-G	UpSco
2MASS J16060391 – 2056443	M8.5	0.12 ± 0.01	0.22 ± 0.01	NA	0.06 ± 0.01	22– –/ VL-G	UpSco
2MASS J16060629 – 2335133	M9.5	0.24 ± 0.01	0.27 ± 0.04	0.10 ± 0.03	0.14 ± 0.02	22–2 / VL-G	UpSco
2MASS J11085497 – 7632410	M8.0	0.03 ± 0.01	0.17 ± 0.01	NA	<0.03	22– – / VL-G	Cha I
2MASS J11123099– 7653342	M7.0	0.09 ± 0.01	0.02 ± 0.04	<0.03	<0.03	22–2 / VL-G	Cha I
2MASS J11074656 – 7615174	M8.0	0.04 ± 0.01	0.18 ± 0.01	NA	NA	22– – / VL-G	Cha I
2MASS J11062554 – 7633418	M8.0	0.05 ± 0.01	0.17 ± 0.02	0.04 ± 0.01	<35.74	222 – / VL-G	Cha I

Note. [a]GS: gravity scores calculated as in Allers & Liu (2013). [b]Gravity scores are ordered according to the alkali line that they correspond to. The dash symbol indicates that no gravity score can be determined with that particular line. [c]OC/A: Open cluster/association to which the target belongs.

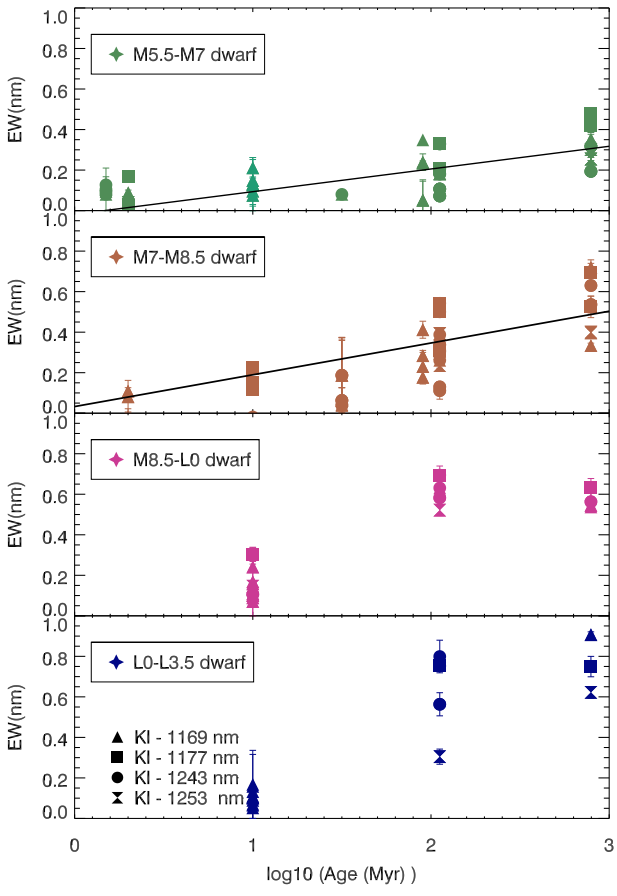

Figure 3. Age versus pEWs of the K I alkali lines in the *J* band (line at 1169 nm as triangles, line at 1177 nm as squares, line at 1243 nm as circles, and line at 1253 nm as hourglasses) of objects in our sample and members of α Persei, of UppSco, of Taurus, and from ρ Ophiuchi, from Martín et al. (2017).

and brown dwarfs has been well defined in the literature (Kirkpatrick et al. 1999; Cushing, Rayner & Vacca 2005; Burgasser et al. 2006, and references therein), in contrast to the spectral classification for young low-mass stars and brown dwarfs.

4.2 Spectral characteristics

4.2.1 Pseudo-equivalent widths of alkali lines

Surface gravity has been found to be correlated with the pseudo-equivalent widths (pEWs) of the alkali lines (Steele & Jameson 1995; Martín et al. 1996; Gorlova et al. 2003; Cushing et al. 2005; Allers et al. 2007; Allers & Liu 2013; Bonnefoy et al. 2014a, and references therein).

To estimate the relative surface gravities of our sample, we measured the pEWs of the following alkali lines in the optical: Rb I (794.8 nm), Na I (818.3 nm), Na I (819.5 nm) and Cs I (852.0 nm). We also measured the Li I line (670.8 nm) and the Hα line (656.3 nm). In the near-infrared, we measured the 1169.2-, 1177.8-, 1243.7- and 1252.9-nm K I lines. These lines are blended with FeH, Fe I and H_2O features in the *J* band for objects with spectral types similar to those in our sample, which might constrain the reliability of these features as age indicators. We measured the pEWs using the same pseudo-continuum windows as defined in Allers & Liu (2013) for the alkali lines in the near-infrared. For alkali lines in the optical, we used the windows shown in Table 3.

In Figs 1 and 2 we present the pEWs of the alkali lines in the optical and in the near-infrared for objects in our sample with ages from 2 to 590–790 Myr belonging to the low-gravity, intermediate-gravity and field-gravity classes defined in Allers & Liu (2013). In Tables 4 and 5 we present the pEW measured values for the alkali lines. For the near-infrared, we overplotted field objects (McLean et al. 2003; Cushing et al. 2005), objects that belong to the TW Hydrae Association (TWA), young companions (Allers & Liu 2013; Bonnefoy et al. 2014b), and young β dwarfs and γ dwarfs as a comparison (Allers & Liu 2013). In addition, we include high-

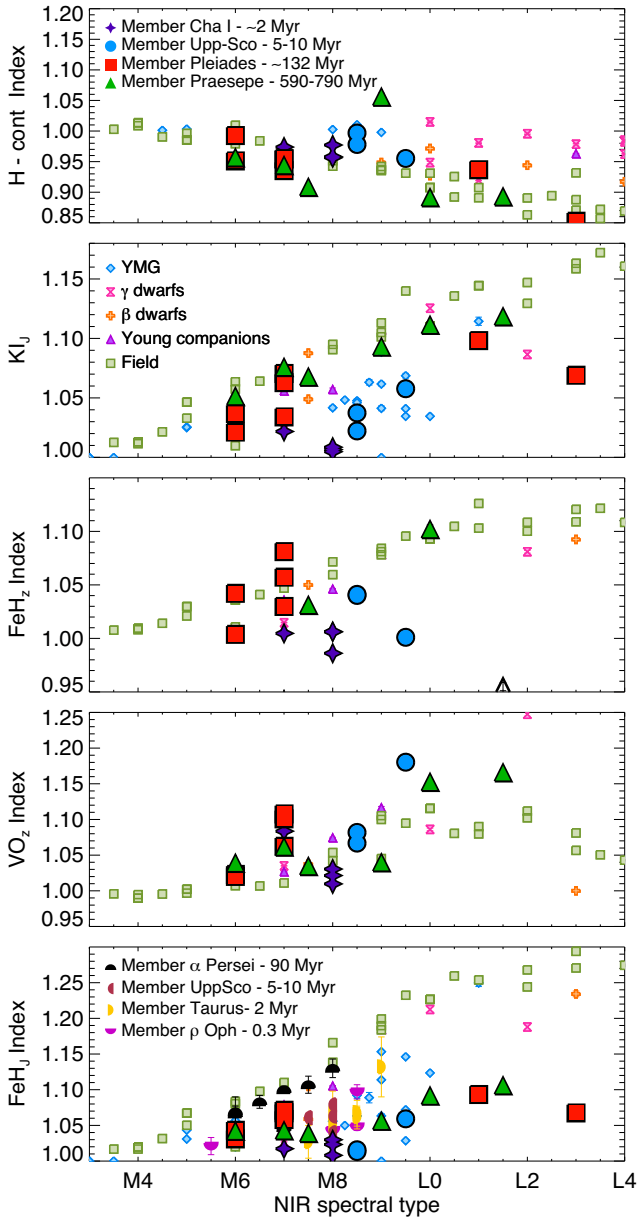

Figure 4. FeH$_J$, KI$_J$ and H-continuum indices from Allers & Liu (2013) for objects in our sample. We overplot field objects (McLean et al. 2003; Cushing et al. 2005), members of the TW Hydrae Association (TWA), young companions (Allers et al. 2007; Bonnefoy et al. 2014b), young β dwarfs and γ dwarfs as a comparison (Allers et al. 2007). We include the value of the FeH index for members of α Persei, of UppSco, of Taurus, and from ρ Ophiuchi (Martín et al. 2017).

probability members of open clusters from Martín et al. (2017), namely five objects from α Persei (90 $\pm$ 10 Myr; Stauffer et al. 1999; Barrado y Navascués 2004), seven from ρ Ophiuchi ($0.3^{+2.7}_{-0.2}$ Myr; Wilking et al. 2005), two from TWA (10 $\pm$ 3 Myr; Mamajek 2005), 13 from Taurus (1.5 $\pm$ 0.5 Myr; Briceño et al. 2002) and 12 from the UppSco association (5−10 Myr).

In the optical, we found Hα emission at 656.3 nm for at least 12 of the 20 objects, most of them with ages up to 132 $\pm$ 27 Myr, indicating chromospheric activity (Stauffer & Hartmann 1986). In addition, we detected lithium in absorption at 670.8 nm in the four Cha I members and the UppSco objects, indicating that no fusion processes have taken place in the interiors at the age of the association. We do not detect Li in any of the Pleiades members, probably because of the low resolution of the OSIRIS/GTC spectra.

As expected, we found that the alkali lines present in the optical spectra (Rb I at 794.8 nm, Na I at 818.3 nm, Na I at 819.5 nm and Cs I at 852.0 nm, see Fig. 1) are weaker for younger objects (see blue points and violet stars belonging to targets from UppSco and Cha I, respectively). Members of the Praesepe open cluster and of the Pleiades have nearly similar pEWs for the alkali lines, even though the Pleiades (132 $\pm$ 27 Myr) is much younger than the Praesepe (590−790 Myr). That would suggest that gravity does not change much after the age of the Pleiades, and therefore we can consider that low-mass stars and more massive brown dwarfs have nearly approached their final radii after their first ∼100 Myr. This tendency agrees with predictions of evolutionary models (Baraffe et al. 2015) that estimate a decrease in radii for a dwarf of 60 M$_{\rm Jup}$ by a factor of 4.4 between 1 and 100 Myr. Between 100 Myr and 3 Gyr, the predicted decrease in radius is a factor of 1.8, which translates to a change in surface gravity from 3.8 dex for very young objects to 4.9 dex for objects of ∼100 Myr and to 5.3 dex for objects older than a few hundred Myr.

In the near-infrared (see Fig. 2), we observe that the alkali lines are weaker for younger objects in general. It can be seen that objects belonging to α Persei (∼90 Myr), the Pleiades (132 $\pm$ 27 Myr) and Praesepe (590−790 Myr) have similar pEWs for all K I alkali lines, confirming the tendency found in the optical that suggests that gravity does not increase significantly after ∼100 Myr. The M and L dwarfs belonging to the Pleiades have slightly weaker pEWs in the near-infrared than do field objects.

In addition, it can be seen that the increase of the pEWs is steeper for objects with spectral type later than M8, where the increases in pEWs quadruple from the youngest to the oldest objects (see Section 4.2.2). Therefore, it is only for objects later than M8 that the pEWs of the alkali lines in the J band might be useful age indicators. An extra challenge when we aim to use alkali lines in the J band as age tracers is the existence of remaining features from the telluric correction, and the blending of these lines with some other spectroscopic features, such as the FeH, Fe I and H_2O, which might introduce extra noise in the measurements of those lines. We find that the best line as gravity/age tracer in the near-infrared is the K I line at 1253 nm, in agreement with Martín et al. (2017) and Lodieu et al. (2018), for which the pEWs have uncertainties of between 5 and 10 per cent.

Finally, we obtained the gravity scores corresponding to each object as described by Allers & Liu (2013). For each near-infrared spectral type, they defined intervals of values of pEWs of the K I lines in the J band that correspond to VL-G, INT-G and FLD-G objects (see table 10 of Allers & Liu 2013). A gravity score of '0' is the index of an object classified as an old field dwarf. A score of '1' indicates intermediate surface gravity. Finally, a score index of '2' means that the pEW or index indicates low surface gravity. The values of the pEW or indices that define each category can be found in tables 9 and 10 of Allers & Liu (2013). The final gravity score is calculated as a median of all the scores. The field-gravity objects have a final score of $\leq$ 0.5. The intermediate-gravity objects have a median gravity score of 1. Finally, objects with a median gravity of $\geq$ 1.5 belong to the very-low-gravity object category. In Table 5, we show the gravity scores obtained for our sample.

The gravity scores classified correctly very-low-gravity objects (belonging to UppSco and Cha I), but Praesepe and Pleiades objects have mixed field- and intermediate-surface-gravity classifications

Table 6. Tentative linear relationship between the pEWs of all the alkali lines and $\log_{10}$(Age) [Myr] plots as shown in Fig. 3.

Sp. type range	Polynomial		χ^2_{red}	Kendall τ coeff.	Significance
	c_0	c_1			
M5.5–M7.0	0.1383 ± 0.0177	8.9477 ± 0.1321	339.4	0.62	1.94e-5
M7.0–M8.5	−0.1809 ± 0.0046	8.7026 ± 0.0462	987.5	0.63	0.0

Note. The polynomials are defined as: $\log_{10}(\text{Age}) = c_0 + c_1 \times \text{pEW}$.

Table 7. Gravity scores for our sample derived from spectral indices defined in the literature (Allers & Liu 2007).

Name	Sp. type	FeH_J	KI_J	H-cont	FeH_z	VO_z	GS[a]	Member
UGCS J083748.00 + 201448.5	M6.0	1.042 ± 0.001	1.051 ± 0.001	0.956 ± 0.002	0.873 ± 0.002	1.038 ± 0.002	1002–/ FLD-G	Praesepe
2MASS J08370215 + 1952074	M7.5	1.038 ± 0.001	1.067 ± 0.001	0.908 ± 0.005	1.031 ± 0.001	1.034 ± 0.002	2002– / INT-G	Praesepe
UGCS J083654.60 + 195415.7	M7.0	1.042 ± 0.001	1.075 ± 0.002	0.943 ± 0.005	0.942 ± 0.003	1.061 ± 0.003	2002– / INT-G	Praesepe
2MASS J08410852 + 1954018	M9.0	1.056 ± 0.001	1.092 ± 0.002	1.055 ± 0.006	0.922 ± 0.003	1.039 ± 0.003	2002– / INT-G	Praesepe
2MASS J08370450 + 2016033	L0.0	1.091 ± 0.002	1.111 ± 0.004	0.891 ± 0.001	1.102 ± 0.004	1.152 ± 0.004	20200 / FLD-G	Praesepe
UGCS J084510.65 + 214817.0	L1.5	1.105 ± 0.002	1.118 ± 0.003	0.892 ± 0.003	0.956 ± 0.003	1.165 ± 0.004	20000 / FLD-G	Praesepe
2MASS J03484469 + 2437236	M6.0	1.031 ± 0.001	1.021 ± 0.001	0.993 ± 0.002	1.003 ± 0.001	1.023 ± 0.002	2202– / VL-G	Pleiades
2MASS J03491512 + 2436225	M6.0	1.043 ± 0.001	1.037 ± 0.001	0.951 ± 0.001	1.042 ± 0.001	1.020 ± 0.002	1101– / INT-G	Plei
2MASS J03512557 + 2345214	M7.0	1.067 ± 0.002	1.071 ± 0.002	0.954 ± 0.001	1.081 ± 0.001	1.101 ± 0.002	1001– / FLD-G	Pleiades
2MASS J03443516 + 2513429	M7.0	1.071 ± 0.002	1.062 ± 0.002	0.935 ± 0.001	1.057 ± 0.001	1.108 ± 0.003	1001– / FLD-G	Pleiades
2MASS J03463425 + 2350036	L1.0	1.093 ± 0.002	1.098 ± 0.004	0.937 ± 0.003	0.899 ± 0.005	1.287 ± 0.006	21022 / INT-G	Pleiades
2MASS J03461406 + 2321565	M7.0	1.058 ± 0.001	1.034 ± 0.002	0.954 ± 0.001	1.029 ± 0.001	1.062 ± 0.002	1202– / INT-G	Pleiades
2MASS J03541027 + 2341402	L3.0	1.067 ± 0.002	1.069 ± 0.002	0.853 ± 0.004	0.819 ± 0.002	1.341 ± 0.002	22022 / VL-G	Pleiades
2MASS J15591135 – 2338002	M8.5	1.016 ± 0.001	1.037 ± 0.001	0.978 ± 0.003	1.040 ± 0.002	1.067 ± 0.002	2212– / VL-G	UpSco
2MASS J16060391 – 2056443	M8.5	1.013 ± 0.001	1.022 ± 0.001	0.996 ± 0.002	1.041 ± 0.001	1.081 ± 0.002	2222– / VL-G	UpSco
2MASS J16060629 – 2335133	M9.5	1.059 ± 0.002	1.057 ± 0.002	0.955 ± 0.002	1.00 ± 0.001	1.180 ± 0.003	2112– / VL-G	UpSco
2MASS J11085497 – 7632410	M8.0	1.008 ± 0.001	1.006 ± 0.001	0.958 ± 0.002	0.986 ± 0.001	1.031 ± 0.001	2202– / VL-G	Cha I
2MASS J11123099 – 7653342	M7.0	1.017 ± 0.001	1.022 ± 0.001	0.974 ± 0.002	1.005 ± 0.001	1.084 ± 0.001	2202– / VL-G	Cha I
2MASS J11074656 – 7615174	M8.0	1.030 ± 0.001	1.005 ± 0.001	0.977 ± 0.002	1.006 ± 0.001	1.021 ± 0.001	2222– / VL-G	Cha I
2MASS J11062554 – 7633418	M8.0	1.023 ± 0.001	1.008 ± 0.001	0.956 ± 0.001	1.001 ± 0.001	1.010 ± 0.001	2202– / VL-G	Cha I

Note. [a]GS: gravity scores calculated as in Allers & Liu (2013)

(see Table 5). Thus, these gravity scores do not always predict the surface gravity expected for the members of each of the clusters/associations that we consider in this study.

4.2.2 *Correlation between ages and alkali lines in the near-infrared*

In Fig. 3, we plot the age of objects in our sample in logarithmic scale versus the pEWs of the K I lines in the *J* band. We add objects with spectral types from M5.5 and L3.5 with well-determined ages from Martín et al. (2017). As suggested by visual inspection in Figs 1 and 2, the pEWs of the alkali lines increase from earlier to later spectral types. Within each spectral type, the pEWs increase from lower to higher surface gravity. We calculated a Kendall correlation index to probe the correlation between the pEWs for the K I lines in the *J* band and the age. We obtained a Kendall correlation of ∼0.63 with significance very close to 0, indicating that there is a moderate correlation between the pEWs of the alkali lines in the *J* band and the age.

We fitted a first-order polynomial that tentatively relates log (Age) with the pEWs of all the K I lines in the *J* band at 1169, 1177, 1243 and 1253 nm. We did not investigate fits with higher-order polynomials, as the dispersion of the pEWs is remarkable and we just intended to derive a tentative relationship between age and pEWs of the K I lines in the *J* band. We used the IDL routine 'poly_fit.pro'. This routine performs a least-squares fit with optional weighting and returns a vector with the coefficients and its χ^2. We added the pEWs measured by Martín et al. (2017) to the pEW versus age plot, and thus we have M5.5 to L3.5 dwarfs with ages from $0.3^{+2.5}_{-0.2}$ Myr (ρ Oph) to 590−790 Myr (Praesepe), covering the whole VL-G, INT-G and FLD-G classification. In Table 6 we show the best-matching first-order polynomial for M5.5–M7.0 and M7.0–M8.5 spectral types. We do not provide polynomials for the rest of the spectral types because of the lack of objects within those ranges of spectral type.

4.2.3 *Spectral indices and gravity scores*

We calculated the FeH_J, KI_J, FeH_z, VO_z and H-cont spectral indices to estimate surface gravity as defined in Allers & Liu (2013). The FeH_J index at 1200 nm has been found to be correlated with surface gravity (McGovern et al. 2004). The KI_J measures the depth of the K I doublet at 1250 nm. The VO band disappears as surface gravity increments with age owing to condensation effects (Lodders 2002). The shape of the continuum of the *H* band has been found to be affected by surface gravity (Borysow, Jorgensen & Zheng 1997; Bowler et al. 2012). For young objects, the *H* band is usually triangular-shaped, and thus the *H*-cont index measures how much the blue end of the *H* band deviates from a straight line. The *H*-cont is small for high-gravity objects, and close to 1 for young objects.

Using the method presented in Allers & Liu (2013), we determined the spectral indices to determine the gravity scores from the FeH_J, KI_J, FeH_z, VO_z and H-cont indices. However, it is important to note that Lodieu et al. () identified the *H*-cont index as the most sensitive to gravity (or age) after testing several indices in a sample

Table 8. Summary of gravity scores provided by the alkali lines and gravity indices.

Name	NIR sp. type	GS[a]	OC/A[b]
UGCS J083748.00 + 201448.5	M6.0	00–01002– / FLD-G	Praesepe
2MASS J08370215 + 1952074	M7.5	11–12002– / INT-G	Praesepe
UGCS J083654.60 + 195415.7	M7.0	11–12002– / INT-G	Praesepe
2MASS J08410852 + 1954018	M9.0	010012002– / FLD-G	Praesepe
2MASS J08370450 + 2016033	L0.0	11–120200 / INT-G	Praesepe
UGCS J084510.65 + 214817.0	L1.5	01–120000 / FLD-G	Praesepe
2MASS J03484469 + 2437236	M6.0	02–12202– / INT-G	Pleiades
2MASS J03491512 + 2436225	M6.0	00–11101– / INT-G	Pleiades
2MASS J03512557 + 2345214	M7.0	00–001001– / FLD-G	Pleiades
2MASS J03443516 + 2513429	M7.0	00–011001– / FLD-G	Pleiades
2MASS J03463425 + 2350036	L1.0	11–121022 / INT-G	Pleiades
2MASS J03461406 + 2321565	M7.0	12–11202– / INT-G	Pleiades
2MASS J03541027 + 2341402	L3.0	11–222022 / VL-G	Pleiades
2MASS J15591135 – 2338002	M8.5	22–22212– / VL-G	UpSco
2MASS J16060391 – 2056443	M8.5	22– –2222– / VL-G	UpSco
2MASS J16060629 – 2335133	M9.5	22–222112– / VL-G	UpSco
2MASS J11085497 – 7632410	M8.0	22– –2202– / VL-G	Cha I
2MASS J11123099 – 7653342	M7.0	22–22202– / VL-G	Cha I
2MASS J11074656 – 7615174	M8.0	22– –2222– / VL-G	Cha I
2MASS J11062554 – 7633418	M8.0	222–2202– / VL-G	Cha I

Note. [a]GS: gravity scores calculated as in Allers & Liu (2013). [b]OC/A: Open cluster/association to which the target belongs.

of field L dwarfs, young β and γ L dwarfs and L dwarf members of the UppSco association. The gravity scores obtained for the spectral indices for our objects are given in Table 7.

Table 8 summarizes the final gravity scores given by the alkali lines and the gravity indices from Allers & Liu (2013) for each object. Combining all gravity indicators, we obtained in general a consistent gravity classification with the age of the cluster or association. We note, however, that three of the six Praesepe members would be classified as INT-G instead of FLD-G with the spectral indices and gravity scores. Similarly, one member of the Pleiades obtained a VL-G classification, and two of them obtained a FLD-G classification, which would not correspond to the expected gravity classification for the Pleiades.

4.3 Age sequences

We present the age sequences of M7.0–M8.5 brown dwarfs and low-mass stars from our X-shooter sample with wavelengths from 0.6 to 2.5 μm from 2 Myr (corresponding to the VL-G gravity class) to 590−790 Myr (corresponding to the FLD gravity class). We degraded the resolution of our spectra to $R\sim700$ to reduce their noise. Their flux is normalized at 1.226 μm. We applied a positive shift to the spectra to be able to overplot all the age sequence in the same plot. In Fig. 5, we compare the optical and the *J*-, *H*- and *K*-band spectra of 2MASS J11074656 – 7615174 (M8.0 Cha I member, age ∼2 Myr), 2MASS J16060391 – 2056443 (M8.5 UppSco member, 5–11 Myr), 2MASS J035125 + 23452 (M7, Pleiades member, age ∼137 Myr) and 2MASS J08372.13 + 195207.4 (M7.5, Praesepe member, 590−790 Myr).

In Fig. 5, we observe the following evolution of spectral characteristics of M7–M8 dwarfs from younger to older age: in the optical, we do not observe a clear tendency for the TiO (0.71, 0.77 and 0.79 μm) and VO (0.74, 0.76 and 0.84 μm) molecular bands with age, nor for the alkali lines (Rb I at 0.794 μm, Na I at 0.818 and 0.819 μm, and Cs I at 0.852 μm). Allers & Liu (2013) claimed that VO varies slightly with surface gravity for M dwarfs at 1.06 μm, but much less than for L dwarfs. In the near-infrared, we observe that in the *J* band the K I alkali lines doublets (1.169 and 1.177 μm, 1.243 and 1.253 μm) increase their pEW with age (i.e. with an increase of surface gravity). In the *H* band, the FeH (1.59 μm) absorption appears to be deeper with age.

4.4 Spectral type–colour diagram

We plot the near-infrared spectral types of our targets, objects with well-constrained ages from Martín et al. (2017), and members of young moving groups from Faherty et al. (2016) versus their $J - W2$ colour in Fig. 6. Faherty et al. (2016) targets are classified with gravity classes corresponding approximately to intermediate-gravity (β) and low-gravity (γ and δ) objects, respectively. We overplot field dwarfs from Dupuy & Liu (2012) as a comparison. In addition, we overplot as a blue solid line the spectrophotometric relationship of Dupuy & Liu (2012) valid for field dwarfs with its associated rms (dashed lines).

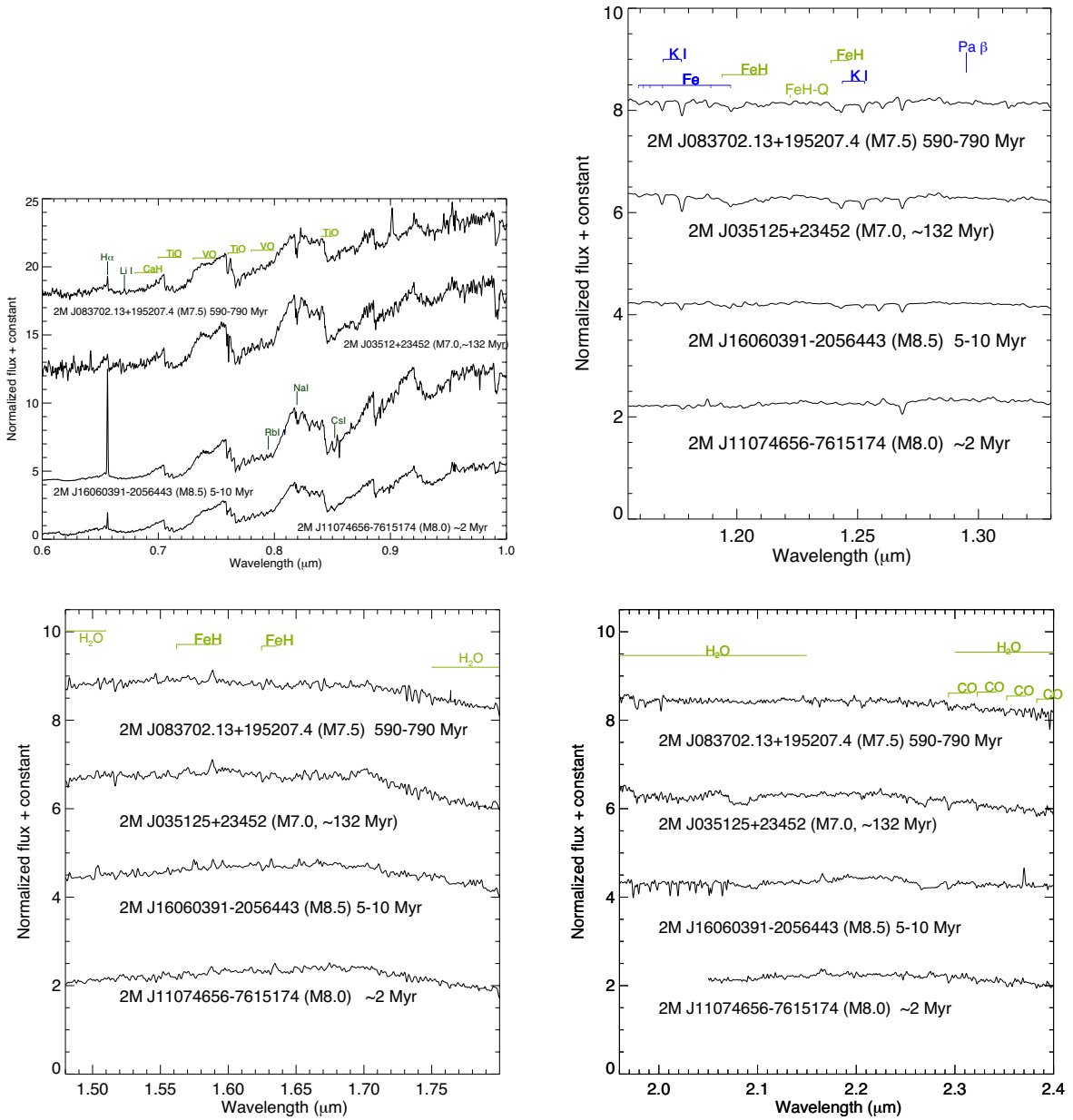

Figure 5. Age sequence of spectra in the optical and near-infrared of M7.0–M8.0 dwarfs with ages from 2 to 790 Myr. The spectral characteristics of M7.0–M8.0 dwarfs are very similar for very young and intermediate-age objects.

We observe that Cha I, ρ Ophiuchi, Taurus and some UppSco members, all below ∼10 Myr, lie above the mean $J - W2$ colours for field M and L dwarfs. Furthermore, objects from Faherty et al. (2016) with spectral types earlier than L0 do not show in general extremely red $J - W2$ colours. In addition, most of their objects with later spectral types show red colours independently of their gravity classification. This suggests that, whatever the cause for red colours in members of young moving groups is, it is probably not a direct indication of the age of the source. It is also important to note that the ages of the sample in Faherty et al. (2016) are estimated using the BANYAN tool (Malo et al. 2013; Gagné et al. 2014), which provides the probability for one object to belong to a young moving group, and thus with an estimated age. The results given by the BANYAN tool should be interpreted with caution, and the resulting ages from that tool should be supported by other indications of young age.[2]

In Fig. 7, we plot ages from 0.3 to 590−790 Myr, in logarithmic scale, versus $J - W2$ colour for four ranges of spectral types: M5.5–M7, M7–M8.5, M8.5–L0 and L0–L3.5. We observe that, in general, colours of brown dwarfs and low-mass stars are bluer with increasing age. Furthermore, on average, after 10 Myr, the average $J - W2$ colour is similar to the $J - W2$ colour for objects that are 590−790 Myr old for objects with a similar spectral type. Table 9 summarizes the Kendall τ coefficient, which shows a moderate

[2]Further details can be found at http://www.astro.umontreal.ca/ gagne/banyanII.php

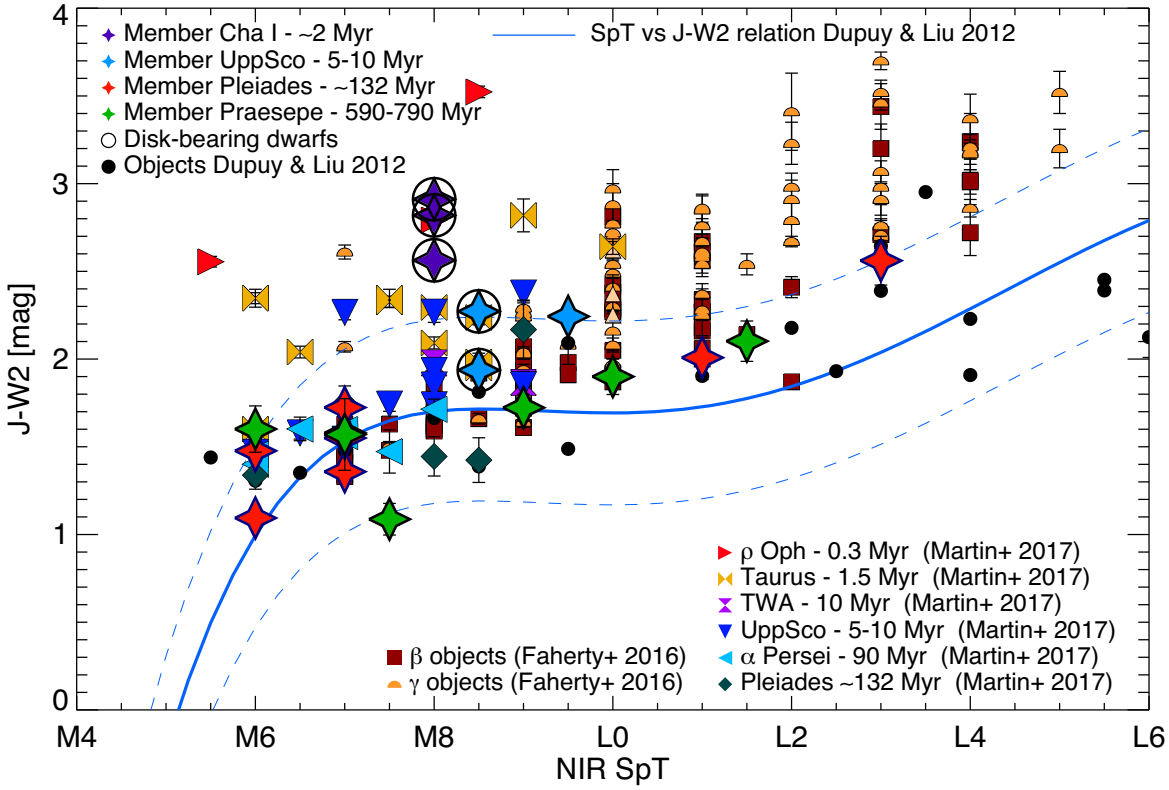

Figure 6. Spectral type versus $J - K$ colour for our sample, dwarfs from Dupuy & Liu (2012), objects with well-determined ages from Martín et al. (2017), and members of young moving groups from Faherty et al. (2016). We overplot circles over the targets that bear discs. The blue line is the spectral–photometric relationship from Dupuy & Liu (2012) for field dwarfs with its typical rms marked with dashed blue lines. Note that only dwarfs with ages younger than 10 Myr show a J–K red colour, lying above the upper rms line.

anticorrelation between the $J - W2$ red colour and age, with τ values ranging from −0.72 for M5.5–M7.0 spectral types to −0.54 for L0.0–L3.5 spectral types. The fact that the red colours do not evolve significantly after 10 Myr suggests that the reddening we observe might be due to circumstellar discs, which can survive up to 10 Myr (Carpenter et al. 2006), at least for objects with the spectral types we consider in this work (M6.0–L3.0). Other explanations for the red colours of some brown dwarfs include the existence of ring structures around these objects (Zakhozhay et al. 2017), extinction through the star-forming region, a viewing angle with inclination >20° (Vos, Allers & Biller 2017), or the presence of submicron particle grains in the atmosphere of L dwarfs, which are probably not included in brown dwarf cloud models with the correct number of particles and opacities (Marocco et al. 2014; Hiranaka et al. 2016; Bonnefoy et al. 2016).

5 PHYSICAL PARAMETERS OF OUR SAMPLE

Owing to the age–mass degeneracy for brown dwarfs, it is challenging to estimate the ages, masses, radii and gravities of brown dwarfs. Nevertheless, if we know the ages, we are able to break the age–mass degeneracy and provide a complete physical characterization of our sample using evolutionary models for low-mass stars and brown dwarfs. This is the aim of this section.

5.1 Bolometric luminosity and bolometric correction

We have optical and near-infrared spectroscopy from X-shooter, or flux-calibrated optical spectroscopy from OSIRIS, and mid-infrared photometry from the WISE (Wide-field Infrared Survey Explorer)catalogue ($W1$ and $W2$) for all the objects in our sample, which allows us to calculate the bolometric luminosity ($L_{\rm bol}$), and the bolometric corrections in the J and K bands ($\rm BC_J$ and $\rm BC_K$). We do not calculate $L_{\rm bol}$ for objects with detected discs: three Cha I members (2MASS J11062554 – 7633418, 2MASS J11074656 – 7615174, 2MASS J11085497 – 7632410) and two UppSco members (2MASS 15591135 – 23380002, 2MASS J16060391 – 2056443).

To calculate the $L_{\rm bol}$, we employed the method presented in Filippazzo et al. (2015), performing a linear interpolation to fill in the gaps left between 0 flux at 0 μm, and the X-shooter optical flux-calibrated spectra. In cases where we did not have an optical spectrum for the source, we filled in the optical wavelengths using its Pan-STARRS optical photometry. Similarly, we interpolated the water bands at 1.4 μm and at 1.8 μm, and the gap between the X-shooter spectra in the near-infrared and the WISE photometry, $W1$ and $W2$. Finally, we interpolated linearly between the reddest WISE photometric point available and 1000 μm, following the procedure of Filippazzo et al. (2015). To calculate the bolometric luminosity of each source, we applied the equation

$$L_{\rm bol} = 4\pi d^2 \int_{0\mu{\rm m}}^{1000\mu{\rm m}} F_\lambda {\rm d}\lambda, \quad (2)$$

where F_λ is the calibrated flux density in units of erg s^{-1}cm$^{-2}\mu$m^{-1}, and d is the distance to the source in centimetres. We present the $L_{\rm bol}$ in Table 10, and plot them versus their near-infrared spectral type in Fig. 8. We overplot the polynomial fit to the spectral type versus

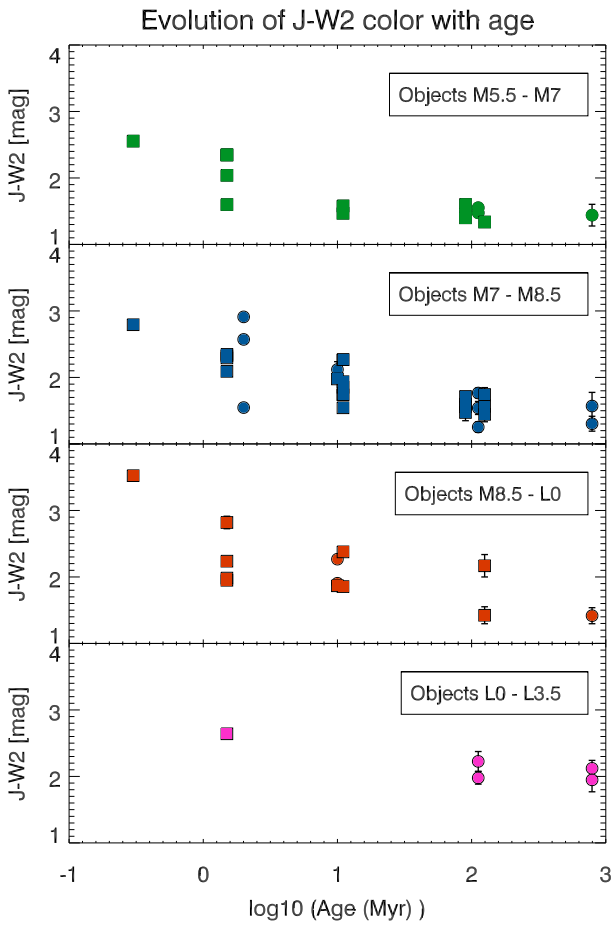

Figure 7. Log(Age) versus $J - W2$ colour for our sample (circles), and objects with well-determined ages from Martín et al. (2017), i.e. members of α Persei, of UppSco, of Taurus, and ρ Ophiuchi (squares), separated by ranges of spectral types.

Table 9. Kendall coefficients indicating the correlation between $J - W2$ and $\log_{10}$(Age [Myr]) plots as shown in Fig. 7.

Sp. type range	Kendall τ coefficient	Significance
M5.5–M7.0	−0.72	1.8e-4
M7.0–M8.5	−0.69	1.8e-7
M8.5–L0.0	−0.54	1.5e-2
L0.0–L3.5	−0.54	1.5e-2

$L_{\rm bol}$ plot from Filippazzo et al. (2015), obtaining similar results for the values of the $L_{\rm bol}$, with the exception of 2MASS J11123099 – 765334 from Cha I, and 2MASS J16060629 – 2335133 from UppSco, which are young objects. In addition, the objects UGCS J083748.00 + 201448.5, 2MASS J08410852 + 1954018, 2MASS J08370450 + 2016033 and UGCS J084510.65 + 214817.0 from the Praesepe, and objects 2MASS J03484469 + 2437236 and 2MASS J03443516 + 2513429 from the Pleiades open cluster are also overluminous, as expected, given that they are binary candidates (see Table 1).

In addition, we calculated the bolometric correction for our sample using the equation

$$BC_{\rm band} = M_{\rm bol} - M_{\rm band}. \quad (3)$$

In Figs 9 and 10, we compare our results with the BCs obtained using the polynomial fit derived by Filippazzo et al. (2015), obtaining in general a consistency between our BCs and the BCs obtained using the polynomial published in Filippazzo et al. (2015). The values obtained for the BCs for our sample are shown in Table 10. This suggests that the binary candidates, if confirmed, might have two components with similar spectral types, to have BCs consistent with a single component.

5.2 Mass, radii, effective temperature and surface gravity

We use the extension of the evolutionary models from Baraffe et al. (2015) for brown dwarfs and extrasolar planets to estimate the values of the masses, effective temperatures, radii and surface gravities for our objects with well-determined ages. In addition, we will compare the values of the surface gravities with the gravity classes defined by Allers & Liu (2013). Because not all grids for all ages are available, we use the closest one in age for the estimation of the physical parameters of our objects: for members of Cha I (∼2 Myr), we use the grid for 2 Myr; for members of UppSco (5−10 Myr), we use the 10-Myr grid; for the Pleiades (132 ± 27 Myr), we use the 120-Myr grid; and for members of the Praesepe (590−790 Myr), we use the 625-Myr grid. In Table 11 , we show the values of the masses, effective temperatures, radii, surface gravities, gravity scores and gravity classes calculated as described in Allers & Liu (2013).

After removing binary candidates, we used evolutionary models to predict the masses for our sample (see Table 11). We estimated masses between 15.2 ± 1.1 $M_{\rm Jup}$ and 113.6 ± 21.4 $M_{\rm Jup}$. Most of our objects, apparently single, have masses below the hydrogen-burning limit. We estimated radii between 1.11 ± 0.14 $R_{\rm Jup}$ and 3.75 ± 0.01 $R_{\rm Jup}$, and surface gravities between 3.51 ± 0.01 and 5.22 ± 0.01 dex. The Praesepe members have surface gravities higher than log g ∼ 5.20 dex, consistent with a FLD-G gravity classification. The Pleiades members have surface gravities of log g ∼ 4.79–4.92 dex, consistent with INT-G to FLD-G classification. The UppSco members have log g ∼ 4.07 dex, consistent with VL-G to INT-G surface gravity classification. Finally, the Cha I member has log g ∼ 3.51 dex, consistent with a VL-G gravity classification.

6 CONCLUSIONS AND FINAL REMARKS

We obtained 0.6−2.5 μm VLT/X-shooter spectra of 20 low-mass stars and brown dwarf members of the Cha I (2 Myr), UppSco (5−10 Myr), Pleiades (132 ± 27 Myr) and Praesepe (590−790 Myr) open clusters. Our targets have spectral types between M6.0 and L3.0.

We performed a consistent spectral classification of our targets by comparing their optical and near-infrared spectra with both young and field M and L templates in both wavelength ranges independently. We obtained a consistent spectral type for most of our objects in all the comparisons, with a maximum discrepancy of ±2.5 spectral types. The maximum dispersion in spectral type classification was reached for very young or field objects, for which the match to field or young objects respectively was more challenging to find. Finally, we adopted the spectral type obtained when comparing with near-infrared field objects as their final spectral classification.

Table 10. Bolometric luminosity and bolometric correction for our targets in the *J* and *K* bands.

Name	Sp. type	*Gaia* π[a] [mas]	log ($L_{bol}/L_{\odot}$)	BC_K	BC_J
UGCS J083748.00 + 201448.5	M6.0	3.53 ± 2.01	−2.95 ± 0.06	2.92 ± 0.16	1.77 ± 0.16
2MASS J08370215 + 1952074	M7.5	3.78 ± 0.80	−2.68 ± 0.09	2.99 ± 0.24	1.92 ± 0.24
UGCS J083654.60 + 195415.7	M7.0		−3.25 ± 0.13	2.87 ± 0.33	1.99 ± 0.33
2MASS J08410852 + 1954018	M9.0		−2.86 ± 0.06	2.99 ± 0.17	2.08 ± 0.17
2MASS J08370450 + 2016033	L0.0		−3.08 ± 0.06	3.22 ± 0.16	1.79 ± 0.16
UGCS J084510.65 + 214817.0	L1.5		−3.24 ± 0.09	3.28 ± 0.22	1.77 ± 0.22
2MASS J03484469 + 2437236	M6.0	6.81 ± 0.34	−2.57 ± 0.02	2.89 ± 0.04	1.84 ± 0.04
2MASS J03491512 + 2436225	M6.0	7.43 ± 0.45	−2.79 ± 0.02	2.99 ± 0.05	1.92 ± 0.05
2MASS J03512557 + 2345214	M7.0	4.38 ± 1.35[b]	−3.09 ± 0.03	2.89 ± 0.08	1.96 ± 0.08
2MASS J03443516 + 2513429	M7.0	7.95 ± 0.98	−2.91 ± 0.02	3.03 ± 0.06	1.91 ± 0.06
2MASS J03463425 + 2350036	L1.0		−3.50 ± 0.08	3.04 ± 0.21	1.79 ± 0.21
2MASS J03461406 + 2321565	M7.0	7.22 ± 0.58	−2.91 ± 0.03	2.86 ± 0.08	1.92 ± 0.08
2MASS J03541027 + 2341402	L3.0		−3.86 ± 0.10	3.52 ± 0.23	1.81 ± 0.23
2MASS J16060629 – 2335133	M9.5		−3.05 ± 0.08	3.18 ± 0.19	1.80 ± 0.19
2MASS J11123099 – 7653342	M7.0		−1.97 ± 0.02	2.72 ± 0.05	1.93 ± 0.05

Notes. [a]When the parallax for the individual object is not available, we use the average parallax to the open cluster/association to calculate the bolometric luminosity, as provided in Section 2.
[b]2MASS J03512557 + 2345214 has a significantly different *Gaia* parallax from the other Pleiades members; thus, it might not be a member of the Pleiades open cluster.

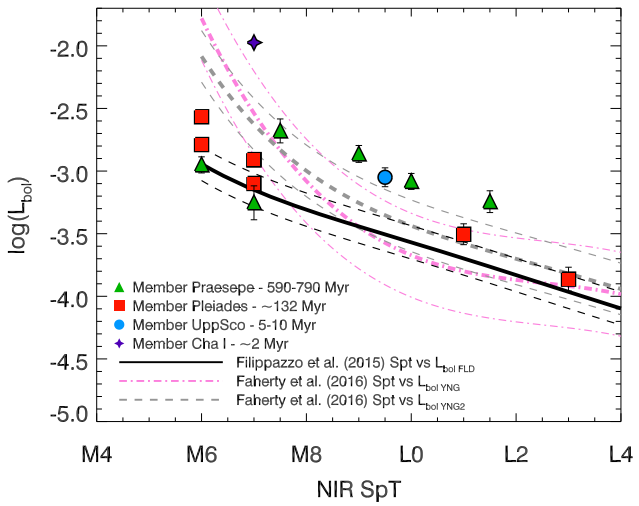

Figure 8. L_{bol} calculated for our sample following the procedure presented in Filippazzo et al. (2015). The grey solid line represents the empirical relationship derived in the same work for spectral type versus L_{bol}, and the grey dashed lines delimit the rms of the empirical relationship.

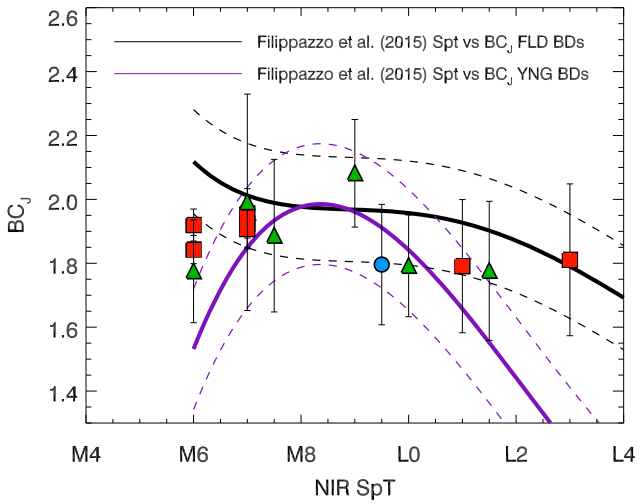

Figure 9. BC_J calculated for our sample following the procedure presented in Filippazzo et al. (2015). The black solid line represents the empirical relationship derived in the same work for spectral type versus BC_J, and the black dashed lines delimit the rms of the empirical relationship. The purple solid line with its respective purple dashed lines represent the same relationship for young brown dwarfs.

We measured the pEWs of the alkali lines in the optical and in the near-infrared. For completeness, we added other measurements for other objects with different ages (see Section 4.2.1). We found that the pEWs of the alkali lines in the optical and near-infrared increase with age, as found in previous works (Steele & Jameson 1995; Martín et al. 1996; Gorlova et al. 2003; Cushing et al. 2005; Allers & Liu 2007, and references therein). We found that members of the Pleiades have similar pEWs for most of the alkali lines than field objects. The same is observed for objects of the α Persei group (90 Myr). This fact suggests that at approximately 100 Myr, low-mass stars and brown dwarfs have nearly reached their final surface gravities, as concluded by Martín et al. (2017), and as predicted by evolutionary models for brown dwarfs (Baraffe et al. 2015).

In addition, we further investigated the relationship between the pEWs of the alkali lines in the near-infrared and age. We found a moderate correlation between the pEWs of the alkali lines in the *J* band and age, for all ranges of spectral types. We observed that the increase of the pEWs with age is more pronounced for objects with spectral type later than M8. We have provided relationships between pEWs and age that can be used in the future to roughly estimate ages given the pEWs of the alkali lines in the *J* band.

We calculated the gravity scores defined by Allers & Liu (2007) using the alkali lines in the *J* band, and the FeH_J, the KI_J, the *H*-cont, the FeH_z and the VO_z band. We obtained a final surface gravity classification, using all the indices, that reproduces reasonably well the youngest objects (Cha I and UppSco) but does not predict accurately intermediate and field M and L dwarfs. Thus, surface gravity indices must be used with caution, especially when a non-low-surface gravity classification is obtained. Red colours have been believed to be a potential indicator of young age and low surface

Table 11. Masses, effective temperatures, surface gravities and radii given by the evolutionary models of Baraffe et al. (2015). We exclude binary candidates and targets with reported circumstellar discs from this list.

Name	Sp. type	M [M_{Jup}]	T_{eff} [K]	R [R_{Jup}]	log g	GC[a]	OC/A[b]
UGCS J083748.00 + 201448.5	M7.0	113.6 ± 21.4	2898 ± 210	1.33 ± 0.20	5.22 ± 0.06	FLD-G	Praesepe
UGCS J083654.60 + 195415.7	M8.0	91.2 ± 15.3	2590 ± 320	1.11 ± 0.14	5.29 ± 0.04	INT-G	Praesepe
2MASS J03491512 + 2436225	M6.0	70.3 ± 3.0	2723 ± 33	1.46 ± 0.03	4.92 ± 0.01	INT-G	Pleiades
2MASS J03443516 + 2513429	M8.5	61.7 ± 6.5	2621 ± 76	1.40 ± 0.03	4.91 ± 0.01	FLD-G	Pleiades
2MASS J03463425 + 2350036	L1.0	37.0 ± 4.5	2017 ± 192	1.23 ± 0.02	4.80 ± 0.03	INT-G	Pleiades
2MASS J03461406 + 2321565	M6.0	56.6 ± 4.7	2537 ± 72	1.36 ± 0.04	4.90 ± 0.01	INT-G	Pleiades
2MASS J03541027 + 2341402	L3.0	36.2 ± 2.3	1983 ± 100	1.22 ± 0.01	4.79 ± 0.02	VL-G	Pleiades
2MASS J16060629–2335133	M9.5	15.2 ± 1.1	2238 ± 55	1.84 ± 0.12	4.07 ± 0.02	VL-G	UpSco
2MASS J11123099–7653342	M7.0	27.3 ± 1.6	2653 ± 21	3.75 ± 0.01	3.51 ± 0.14	VL-G	Cha I

Note. [a]GS: gravity scores as described in Allers & Liu (2013). The first three gravity scores belong to the result of the pEWs of the K I lines at 1169, 1177 and 1253 nm. The rest belong to the gravity scores obtained from the spectral indices described in Section 4.2.3. [b]OC/A: open cluster/association to which the target belongs

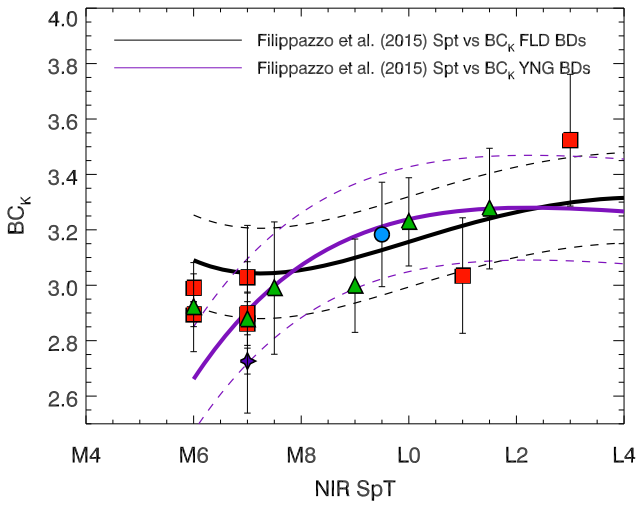

Figure 10. BC$_K$ calculated for our sample following the procedure presented in Filippazzo et al. (2015). The black solid line represents the empirical relationship derived in the same work for spectral type versus BC$_K$, and the black dashed lines delimit the rms of the empirical relationship. The purple solid line with its respective purple dashed lines represent the same relationship for young brown dwarfs.

gravity (Allers & Liu 2013; Bonnefoy et al. 2014a; Manjavacas et al. 2014, and references therein). Thus, we investigated the correlation between the $J - W2$ colour and age. We found a moderate correlation between these two quantities for the spectral types we considered in our work. In Figs 6 and 7, we found that objects that were mostly red have ages younger than ∼10 Myr; this might be linked to the existence of a protoplanetary disc, ring structures, extinction through the star-forming region, or viewing angle, but not necessarily to the influence of low surface gravity in their atmospheres. In addition, some of the members of moving groups older than 100 Myr presented in Faherty et al. (2016) show very red colours. This fact suggests that colours do not scale linearly with age (Marocco et al. 2014; Liu, Dupuy & Allers 2016; Bowler et al. 2017; Zapatero Osorio et al. 2017).

We calculated the bolometric luminosity of our sample using the optical, or optical Pan-STARRS photometry, near-infrared X-shooter flux-calibrated spectra, and WISE photometry. We calculated the bolometric corrections in the J and K bands, and compared them with the polynomial fits from Filippazzo et al. (2015) and Faherty et al. (2016). With the exception of binary candidates, most of our targets followed the spectral type versus L_{bol} relationship from Filippazzo et al. (2015). Praesepe and Pleiades non-binary candidate members followed the relationship derived by Filippazzo et al. (2015) for field objects. Members of the Cha I or the UppSco association are overluminous with respect to the field and the young sequence, which is in agreement with expectations for such young sources.

Similarly, we plotted the relationship between near-infrared spectral type and the BC$_J$ and BC$_K$. We overplotted the spectral type versus BC$_J$ and BC$_K$ relationship for field and young objects. All objects of our sample follow these relationships, even binary candidates. This suggests that, in cases where our binary candidates are actual binaries, their components should have similar spectral type, so that the difference between the absolute flux in the J and K bands remains similar to the difference for a single object of the same spectral type.

The surface gravities obtained for our targets using Baraffe et al. (2015) evolutionary models did not always agree with the gravity classification given by Allers & Liu (2013) indices. The gravity classification was consistent only for all objects from the Cha I and from the UppSco association. Thus, as suggested previously, gravity indices should be used with caution, considering that they might not always provide an accurate spectral classification.

ACKNOWLEDGEMENTS

This publication makes use of data products from the Two Micron All Sky Survey, which is a joint project of the University of Massachusetts and the Infrared Processing and Analysis Center/California Institute of Technology, funded by the National Aeronautics and Space Administration and the National Science Foundation

The work is based on observations (programme GTC66-12B) made with the Gran Telescopio Canarias (GTC), operated on the island of La Palma in the Spanish Observatorio del Roque de los Muchachos of the Instituto de Astrofísica de Canarias, and with observations collected at the EU Organization for Astronomical Research in the Southern Hemisphere under ESO programmes 098.C-0277(A), 0.93.C-0109(A), and 0.95.C-0812(A), 0.93.C-0769(A) and 0.95.C-0378(A).

It has made use of data from the European Space Agency (ESA) mission *Gaia* (https://www.cosmos.esa.int/gaia), processed by the *Gaia* Data Processing and Analysis Consortium (DPAC, https://www.cosmos.esa.int/web/gaia/dpac/consortium). Funding for

the DPAC was provided by national institutions, in particular the institutions participating in the *Gaia* Multilateral Agreement.

NL and VJSB are supported by programme AYA2015-69350-C3-2-P, and MRZO by programme AYA2016-79425-C3-2-P from the Spanish Ministry of Economy and Competitiveness (MINECO).

Based on observations of VLT/XSHOOTER, under the program ID 098.C-0277.

REFERENCES

Allers. L.N., JaffeD.T, Luhman K. L, Liu MIchael C, Wilson J. C., Skrutskie M. F., Nelson M, Peterson D. E., Smith J. D., Cushing M. C., 2007, ApJ, 657, 511
Allers K. N., Liu M. C., 2013, ApJ, 772, 79
Allers K. N. et al., 2007, ApJ, 657, 511
Alves de Oliveira C., Moraux E., Bouvier J., Bouy H., 2012, A&A, 539, A151
Ardila D., Martín E., Basri G., 2000, AJ, 120, 479
Baraffe I., Homeier D., Allard F., Chabrier G., 2015, A&A, 577, A42
Barrado y Navascués D., 2004, in Favata F., Aigrain S., Wilson A., eds, Stellar Structure and Habitable Planet Finding Vol. 538 of ESA Special Publication, The stellar population in the field of the α Persei cluster. p. 269
Best W. M. J. et al., 2017, ApJ, 837, 95
Bihain G., Rebolo R., Béjar V. J. S., Caballero J. A., Bailer-Jones C. A. L., Mundt R., Acosta-Pulido J. A., Manchado Torres A., 2006, A&A, 458, 805
Bihain G., Rebolo R., Zapatero Osorio M. R., Béjar V. J. S., Caballero J. A., 2010, A&A, 519, A93
Blanton M. R., et al., 2017, AJ, 154, 28
Bonnefoy M., Chauvin G., Lagrange A.-M., Rojo P., Allard F., Pinte C., Dumas C., Homeier D., 2014a, A&A, 562, A127
Bonnefoy M., Chauvin G., Lagrange A.-M., Rojo P., Allard F., Pinte C., Dumas C., Homeier D., 2014b, A&A, 562, A127
Bonnefoy M. et al., 2016, A&A, 587, A58
Borysow A., Jorgensen U. G., Zheng C., 1997, A&A, 324, 185
Boudreault S., Lodieu N., 2013, MNRAS, 434, 142
Boudreault S., Bailer-Jones C. A. L., Goldman B., Henning T., Caballero J. A., 2010, A&A, 510, A27
Boudreault S., Lodieu N., Deacon N. R., Hambly N. C., 2012, MNRAS, 426, 3419
Boulanger F., Bronfman L., Dame T. M., Thaddeus P., 1998, A&A, 332, 273
Bouvier J., Stauffer J. R., Martin E. L., Barrado y Navascues D., Wallace B., Bejar V. J. S., 1998, A&A, 336, 490
Bouy H. et al., 2015, A&A, 577, A148
Bowler B. P. et al., 2017, AJ, 153, 18
Bowler B. P., Liu M. C., Shkolnik E. L., Dupuy T. J., Cieza L. A., Kraus A. L., Tamura M., 2012, ApJ, 753, 142
Brandt T. D., Huang C. X., 2015, ApJ, 807, 24
Breger M., 1986, ApJ, 309, 311
Briceño C., Luhman K. L., Hartmann L., Stauffer J. R., Kirkpatrick J. D., 2002, ApJ, 580, 317
Burgasser A. J., Geballe T. R., Leggett S. K., Kirkpatrick J. D., Golimowski D. A., 2006, ApJ, 637, 1067
Burrows A., Marley M., Hubbard W. B., Lunine J. I., Guillot T., Saumon D., Freedman R., Sudarsky D., Sharp C., 1997, ApJ, 491, 856
Carpenter J. M., Mamajek E. E., Hillenbrand L. A., Meyer M. R., 2006, ApJ, 651, L49
Carpenter J. M., Ricci L., Isella A., 2014, ApJ, 787, 42
Cepa J., Bland-Hawthorn J., González J. J., OSIRIS Consortium, 2000, in van Breugel W., Bland-Hawthorn J., eds, Asronomy Society of the Pacific Conference Series Vol. 195, Imaging the Universe in Three Dimensions. Astron. Soc. Pac, San Francisco, p. 597
Chambers K. C. et al., 2016, preprint (arXiv e-prints)
Chauvin G., Lagrange A.-M., Dumas C., Zuckerman B., Mouillet D., Song I., Beuzit J.-L., Lowrance P., 2004, A&A, 425, L29
Chiu K., Fan X., Leggett S. K., Golimowski D. A., Zheng W., Geballe T. R., Schneider D. P., Brinkmann J., 2006, AJ, 131, 2722
Cruz K. L., Kirkpatrick J. D., Burgasser A. J., 2009, AJ, 137, 3345
Cushing M. C., Rayner J. T., Vacca W. D., 2005, ApJ, 623, 1115
Cushing M. C. et al., 2008, ApJ, 678, 1372
Dahm S. E., 2015, ApJ, 813, 108
de Zeeuw P. T., Hoogerwerf R., de Bruijne J. H. J., Brown A. G. A., Blaauw A., 1999, AJ, 117, 354
Deacon N. R., Hambly N. C., 2004, A&A, 416, 125
Delorme P., Collier Cameron A., Hebb L., Rostron J., Lister T. A., Norton A. J., Pollacco D., West R. G., 2011, MNRAS, 413, 2218
Dupuy T. J., Liu M. C., 2012, ApJS, 201, 19
Faherty J. K., Rice E. L., Cruz K. L., Mamajek E. E., Núñez A., 2013, AJ, 145, 2
Faherty J. K. et al., 2016, ApJS, 225, 10
Fang Q., Herczeg G. J., Rizzuto A., 2017, ApJ, 842, 123
Feiden G. A., 2016, A&A, 593, A99
Filippazzo J. C., Rice E. L., Faherty J., Cruz K. L., Van Gordon M. M., Looper D. L., 2015, ApJ, 810, 158
Fossati L., Bagnulo S., Landstreet J., Wade G., Kochukhov O., Monier R., Weiss W., Gebran M., 2008, A&A, 483, 891
Gagné J., Lafrenière D., Doyon R., Malo L., Artigau É., 2014, ApJ, 783, 121
Gaia Collaboration et al., 2018, A&A, 616, A1
Gizis J. E. et al., 2012, AJ, 144, 94
Gizis J. E., Allers K. N., Liu M. C., Harris H. C., Faherty J. K., Burgasser A. J., Kirkpatrick J. D., 2015, ApJ, 799, 203
Golimowski D. A. et al., 2004, AJ, 127, 3516
Gorlova N. I., Meyer M. R., Rieke G. H., Liebert J., 2003, ApJ, 593, 1074
Gossage S., Conroy C., Dotter A., Choi J., Rosenfield P., Cargile P., Dolphin A., 2018, ApJ, 863, 67
Herczeg G. J., Cruz K. L., Hillenbrand L. A., 2009, ApJ, 696, 1589
Hiranaka K., Cruz K. L., Douglas S. T., Marley M. S., Baldassare V. F., 2016, ApJ, 830, 96
Hodgkin S. T., Pinfield D. J., Jameson R. F., Steele I. A., Cossburn M. R., Hambly N. C., 1999, MNRAS, 310, 87
Jones B. F., Stauffer J. R., 1991, AJ, 102, 1080
Kirkpatrick J. D. et al., 1999, ApJ, 519, 802
Kirkpatrick J. D., Barman T. S., Burgasser A. J., McGovern M. R., McLean I. S., Tinney C. G., Lowrance P. J., 2006, ApJ, 639, 1120
Kirkpatrick J. D. et al., 2012, ApJ, 753, 156
Knapp G. R. et al., 2004, AJ, 127, 3553
Kraus A. L., Ireland M. J., Martinache F., Lloyd J. P., 2008, ApJ, 679, 762
Lawrence A. et al., 2007, MNRAS, 379, 1599
Liu M. C. et al., 2013, ApJ, 777, L20
Liu M. C., Dupuy T. J., Allers K. N., 2016, ApJ, 833, 96
Lodders K., 2002, ApJ, 577, 974
Lodieu N., 2013, MNRAS, 431, 3222
Lodieu N., Hambly N. C., Jameson R. F., Hodgkin S. T., Carraro G., Kendall T. R., 2007, MNRAS, 374, 372
Lodieu N., Deacon N. R., Hambly N. C., 2012a, MNRAS, 422, 1495
Lodieu N., Deacon N. R., Hambly N. C., 2012b, MNRAS, 422, 1495
Lodieu N., Zapatero Osorio M. R., Béjar V. J. S., Peña Ramírez K., 2018, MNRAS, 473, 2020
Lodieu N., Pérez-Garrido A., Smart R. L., Silvotti R., 2019, A&A, 628, A66
Long F. et al., 2017, ApJ, 844, 99
López Martí B., Eislöffel J., Scholz A., Mundt R., 2004, A&A, 416, 555
Luhman K. L., 2004, ApJ, 602, 816
Luhman K. L., 2007, ApJS, 173, 104
Luhman K. L., Mamajek E. E., 2010, ApJ, 716, L120
Luhman K. L., Muench A. A., 2008, ApJ, 684, 654
Luhman K. L., Herrmann K. A., Mamajek E. E., Esplin T. L., Pecaut M. J., 2018, AJ, 156, 76
Malo L., Doyon R., Lafrenière D., Artigau É., Gagné J., Baron F., Riedel A., 2013, ApJ, 762, 88
Mamajek E. E., 2005, ApJ, 634, 1385

Mamajek E. E., Lawson W. A., Feigelson E. D., 2000, ApJ, 544, 356
Manara C. F. et al., 2017, A&A, 604, A127
Manjavacas E. et al., 2014, A&A, 564, A55
Marocco F. et al., 2014, MNRAS, 439, 372
Marois C., Macintosh B., Barman T., Zuckerman B., Song I., Patience J., Lafrenière D., Doyon R., 2008, Science, 322, 1348
Martín E. C. et al., 2017, ApJ, 838, 73
Martín E. L., Rebolo R., Zapatero-Osorio M. R., 1996, ApJ, 469, 706
Martín E. L., De.lfosse X., Guieu S., 2004, AJ, 127, 449
Martín E. L., Lodieu N., Pavlenko Y., Béjar V. J. S., 2018, ApJ, 856, 40
McGovern M. R., Kirkpatrick J. D., McLean I. S., Burgasser A. J., Prato L., Lowrance P. J., 2004, ApJ, 600, 1020
McLean I. S., McGovern M. R., Burgasser A. J., Kirkpatrick J. D., Prato L., Kim S. S., 2003, ApJ, 596, 561
Moraux E., Bouvier J., Stauffer J. R., Cuillandre J.-C., 2003, A&A, 400, 891
Nagashima C. et al., 2003, MNRAS, 343, 1263
Netopil M., Paunzen E., Heiter U., Soubiran C., 2016, A&A, 585, A150
Pecaut M. J., Mamajek E. E., 2016, MNRAS, 461, 794
Pecaut M. J., Mamajek E. E., Bubar E. J., 2012, ApJ, 746, 154
Persi P. et al., 2000, A&A, 357, 219
Pinfield D. J., Dobbie P. D., Jameson R. F., Steele I. A., Jones H. R. A., Katsiyannis A. C., 2003, MNRAS, 342, 1241
Prusti T., Clark F. O., Whittet D. C. B., Laureijs R. J., Zhang C. Y., 1991, MNRAS, 251, 303
Rizzuto A. C., Ireland M. J., Dupuy T. J., Kraus A. L., 2016, ApJ, 817, 164
Roccatagliata V., Sacco G. G., Franciosini E., Randich S., 2018, ApJ, 617, L4
Schlieder J. E., Lépine S., Rice E., Simon M., Fielding D., Tomasino R., 2012, AJ, 143, 114
Schneider A. C., Cushing M. C., Kirkpatrick J. D., Mace G. N., Gelino C. R., Faherty J. K., Fajardo-Acosta S., Sheppard S. S., 2014, AJ, 147, 34
Schneider A. C., Windsor J., Cushing M. C., Kirkpatrick J. D., Shkolnik E. L., 2017, AJ, 153, 196
Skrutskie M. F. et al., 2006, AJ, 131, 1163
Slesnick C. L., Hillenbrand L. A., Carpenter J. M., 2008, ApJ, 688, 377
Soderblom D. R., Laskar T., Valenti J. A., Stauffer J. R., Rebull L. M., 2009, AJ, 138, 1292
Song I., Zuckerman B., Bessell M. S., 2012, AJ, 144, 8
Spina L. et al., 2014, A&A, 568, A2
Stauffer J. R., Hartmann L. W., 1986, ApJS, 61, 531
Stauffer J. R., Schultz G., Kirkpatrick J. D., 1998, ApJ, 499, L199
Stauffer J. R. et al., 1999, ApJ, 527, 219
Steele I. A., Jameson R. F., 1995, MNRAS, 272, 630
Stephens D. C. et al., 2009, ApJ, 702, 154
Taylor B. J., 2006, AJ, 132, 2453
Theodossiou E., Danezis E., 1991, Ap&SS, 183, 91
Tody D., 1986, in Crawford D. L., ed., Instrumentation in Astronomy VI, Vol. 627 of Proc. SPIE, The IRAF Data Reduction and Analysis System. p. 733
Tody D., 1993, in Hanisch R. J., Brissenden R. J. V., Barnes J., eds, Astronomical Data Analysis Software and Systems II, Vol. 52 of Astronomical Society of the Pacific Conference Series, IRAF in the Nineties. p. 173, Asron. Soc. Pac, San Francisco
van der Plas G. et al., 2016, ApJ, 819, 102
Vernet J. et al., 2011, A&A, 536, A105
Vos J. M., Allers K. N., Biller B. A., 2017, ApJ, 842, 78
West A. A. et al., 2011, AJ, 141, 97
Wilking B. A., Meyer M. R., Robinson J. G., Greene T. P., 2005, AJ, 130, 1733
Winston E. et al., 2012, A&A, 545, A145
Zakhozhay O. V., Zapatero Osorio M. R., Béjar V. J. S., Boehler Y., 2017, MNRAS, 464, 1108
Zapatero Osorio M. R., Rebolo R., Martin E. L., 1997, A&A, 317, 164
Zapatero Osorio M. R., Béjar V. J. S., Peña Ramírez K., 2017, ApJ, 842, 65

SUPPORTING INFORMATION

Supplementary data are available at *MNRAS* online.

Table A3. Sample of an ASCII table of the online material containing the spectra presented in this work.

Please note: Oxford University Press is not responsible for the content or functionality of any supporting materials supplied by the authors. Any queries (other than missing material) should be directed to the corresponding author for the article.

APPENDIX A:

Table A1. Log of the observed targets with VLT/X-shooter.

Name	Date	Arm	DIT [s]	NINT	Seeing [arcmin]	SNR VIS/NIR	Airmass	Notes
UGCS J083748.00 + 201448.5	Jan 29, 2017	VIS/NIR	305/300	4/4	0.73	1.9/7.2	1.49	
Hip040881	Jan 29, 2017	VIS/NIR.	6.25/30	2/2	0.94		1.55	B9.5V Telluric Standard
2MASS J08370215 + 1952074	Jan 28, 2017	VIS/NIR	305/300	10/7	0.9	3.5/12.1	1.58	
Hip040881	Jan 28, 2017	VIS/NIR	5/10	2/2	0.66		1.62	B9.5V Telluric Standard
UGCS J083654.60 + 195415.7	Jan 23, 2017	VIS/NIR	305/300	10/7	0.83	0.9/4.5	1.51	
Hip043564	Jan 23, 2017	VIS/NIR	40/90	2/2	0.8		1.50	B5V Telluric Standard
J08410852 + 1954018	Jan 23, 2017	VIS/NIR	305/300	8/8	1.02	1.2/7.9	1.41	
Hip043564	Jan 23, 2017	VIS/NIR	40/90	2/2	0.92		1.5	B5V Telluric Standard
2MASS J08370450 + 2016033	Jan 1, 2017	VIS/NIR	305/300	8/8	0.51	1.0/8.2	1.50	
Hip022597	Jan 1, 2017	VIS/NIR	12.5/30	1/1	1.1		1.05	B5V Telluric Standard
UGCS J084510.65 + 214817.0	Jan 2, 2017	VIS/NIR	305/300	10/10	0.6	0.6/5.0	1.46	
Hip026545	Jan 2, 2017	VIS/NIR	12.5/30	2/2	0.74		1.49	B6V Telluric Standard
2MASS J03484469 + 2437236	Nov 30, 2016	VIS/NIR	305/300	6/6	0.67	9.0/24.6	1.53	
Hip009534	Jan 4, 2010	VIS/NIR	6/5	1/1	1.1		1.1	B6V Telluric Standard
2MASS J03491512 + 2436225	Nov 27, 2016	VIS/NIR	305/300	6/6	0.34	6.7/23.2	1.61	
Hip017900	Nov 27, 2016	VIS/NIR	6/10	2/2	0.6		1.51	B8V Telluric Standard
2MASS J03512557 + 2345214	Nov 26, 2016	VIS/NIR	305/300	8/8	0.4	2.8/13.4	1.51	
Hip021013	Nov 26, 2016	VIS/NIR	8/10	2/2	0.45		1.51	B8III Telluric Standard
2MASS J03443516 + 2513429	Nov 20, 2016	VIS/NIR	305/300	6/6	1.22	2.8/18.9	1.82	
Hip022527	Nov 20, 2016	VIS/NIR	12.5/30	2/2	1.0		1.72	B3V Telluric Standard
2MASS J03463425 + 2350036	Nov 11, 2016	VIS/NIR	305/300	10/10	0.28	0.5/5.2	1.58	
Hip020789	Nov 11, 2016	VIS/NIR	6/7	2/2	0.27		1.65	B7V Telluric Standard
2MASS J03461406 + 2321565	Nov 3, 2016	VIS/NIR	305/300	6/14	0.84	4.1/15.4	2.09	
Hip054006	Nov 3, 2016	VIS/NIR	15/23	2/2	0.9		1.91	B5V Telluric Standard
2MASS J03541027 + 2341402	Nov 3, 2016	VIS/NIR	305/300	14/14	1.04	0.1/3.6	1.68	
Hip045125	Nov 3, 2016	VIS/NIR	15/12	2/2	0.77		1.52	B9V Telluric Standard
2MASS J15591135–2338002	Apr 25, 2014	VIS/NIR	866/227.5	3/3	1.64	25.2/21.6	1.09	
Hip079073	Apr 25, 2014	VIS/NIR	20/20	2/2	1.50		1.09	G2V Telluric Standard
2MASS J16060391–2056443	Apr 08, 2014	VIS/NIR	866/27.5	3/3	1.47	38.8/45.7	1.00	
Hip074389	Apr 08, 2014	VIS/NIR	6.5/8	2/2	1.01		1.01	G1.5V Telluric Standard
2MASS J16060629–2335133	Jun 25, 2014	VIS/NIR	197/190	14/14	0.99	2.2/13.8	1.21	
Hip087314	Jun 25, 2014	VIS/NIR	6.25/30	2/2	1.00		1.62	B2/3Vnn Telluric Standard
2MASS J11085497–7632410	May 5, 2015	VIS/NIR	645/245	4/4	1.03	13.0/21.1	1.69	
Hip061066	May 5, 2015	VIS/NIR	25/20	2/2	1.17		1.58	B9V Telluric Standard
2MASS J11123099–7653342	Jan 14, 2017	VIS/NIR	305/300	6/6	0.8	11.5/53.6	1.63	
Hip053024	Jan 14, 2017	VIS/NIR	9/20	2/2	0.75		1.65	B4V Telluric Standard
2MASS J11074656-7615174	Apr 3, 2015	VIS/NIR	585/225	4/4	1.4	30.2/16.4	1.67	
Hip061066	Apr 3, 2015	VIS/NIR	12.5/15	2/2	0.83		1.59	B9V Telluric Standard
Cha J11070768–7626326	Apr 5, 2015	VIS/NIR	585/225	4/4	1.35	17.7/39.4	1.65	
Hip061066	Apr 5, 2015	VIS/NIR	15/20	2/2	1.63		1.58	B9V Telluric Standard

Table A2. Observing log for objects observed with GTC/OSIRIS.

Name	Resolution	Num. exp. × exp. time [s]	Observing date
UGCS J083748.00 + 201448.5	R300R	1 × 900	17 Dec 2012
2MASS J08410852 + 1954018	R300R	1 × 900	15 Dec 2012
UGCS J083654.60 + 195415.7	R300R	3 × 600	03 Feb 2013
2MASS J08370215 + 1952074	R300R	1 × 900	20 Jan 2013
UGCS J084510.65 + 214817.0	R300R	6 × 700	16 Jan 2013
2MASS J08370450 + 2016033	R300R	3 × 700	16 Jan 2013
2MASS J03463425 + 2350036	R300R	3 × 700	17 Jan 2013

Table A3. Sample of an ASCII table of the online material containing the spectra presented in this work. Full tables are available online.

Title: Spectral library of age-benchmark low-mass stars and brown dwarfs
Authors: E. Manjavacas, N. Lodieu, V. J. S. Béjar, M. R. Zapatero-Osorio, S. Boudreault, M. Bonnefoy
Table: object_name

Byte-by-byte Description of file: object_name.txt

Format	Units	Label	Explanations
F7.3	nm	Wave	Wavelength
E11.5	erg/cm^2/s/micron	Flux	Flux density
E11.5	erg/cm^2/s/micron	e_Flux	Uncertainty in flux
550.000	6.99669e-14	1.56783e-13	
550.020	1.87205e-12	−2.33466e-13	
550.040	1.11997e-12	−9.44294e-13	
550.060	1.17393e-12	−1.02712e-12	
550.080	6.04876e-13	1.69853e-13	
550.100	−2.60507e-13	−3.57532e-13	

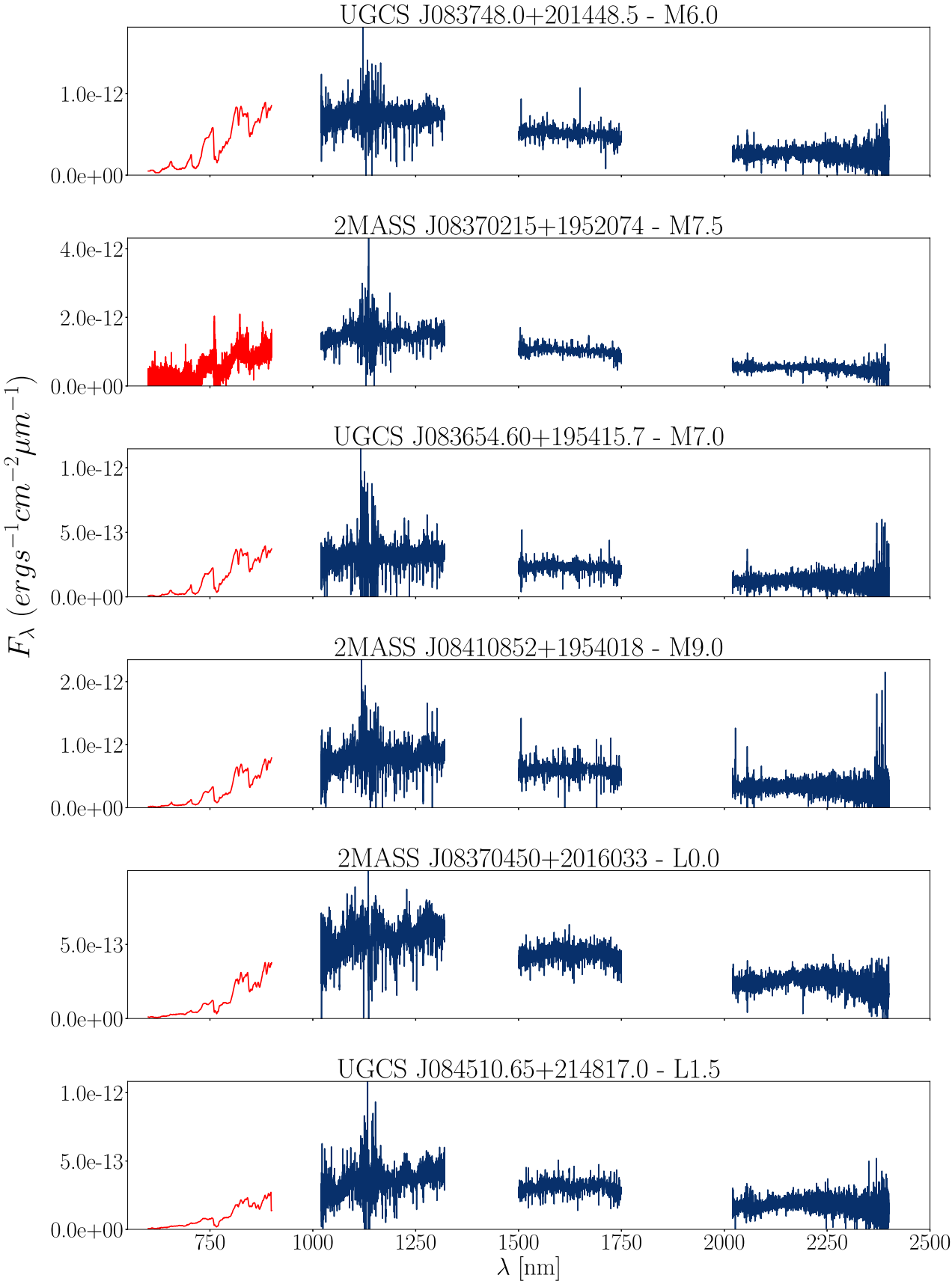

Figure A1. X-shooter/VLT and OSIRIS/GTC spectra for objects from the Praesepe open cluster listed in Table 1. The OSIRIS or X-shooter optical spectra are shown in red for clarity. The flux density is given in F_λ in erg s^{-1}cm$^{-2}\mu$m^{-1}.

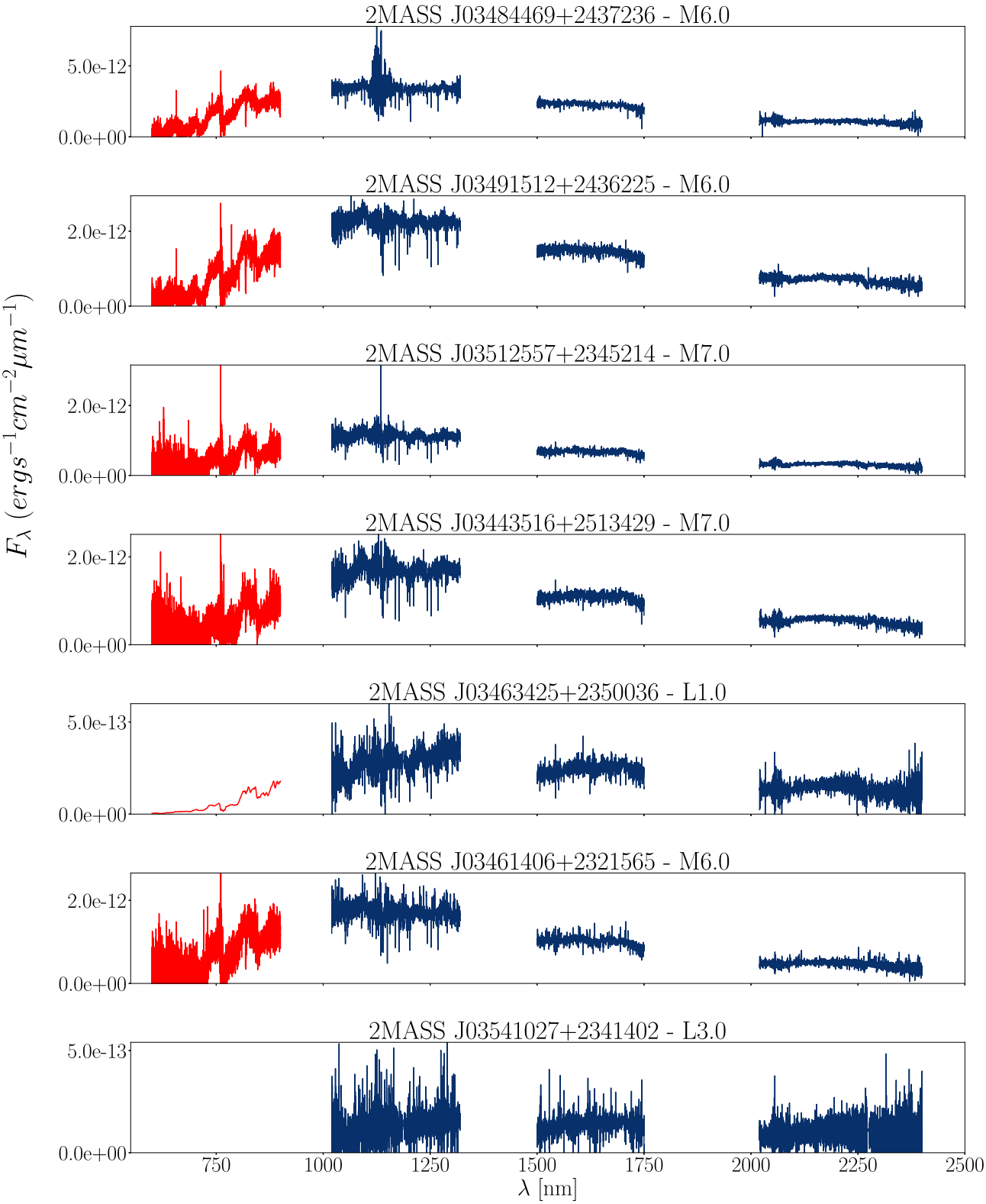

Figure A2. X-shooter/VLT and OSIRIS/GTC spectra for objects from the Pleiades open cluster listed in Table 1. The X-shooter optical spectra are shown in red for clarity. The flux density is given in F_λ in erg s^{-1}cm$^{-2}\mu$m^{-1}.

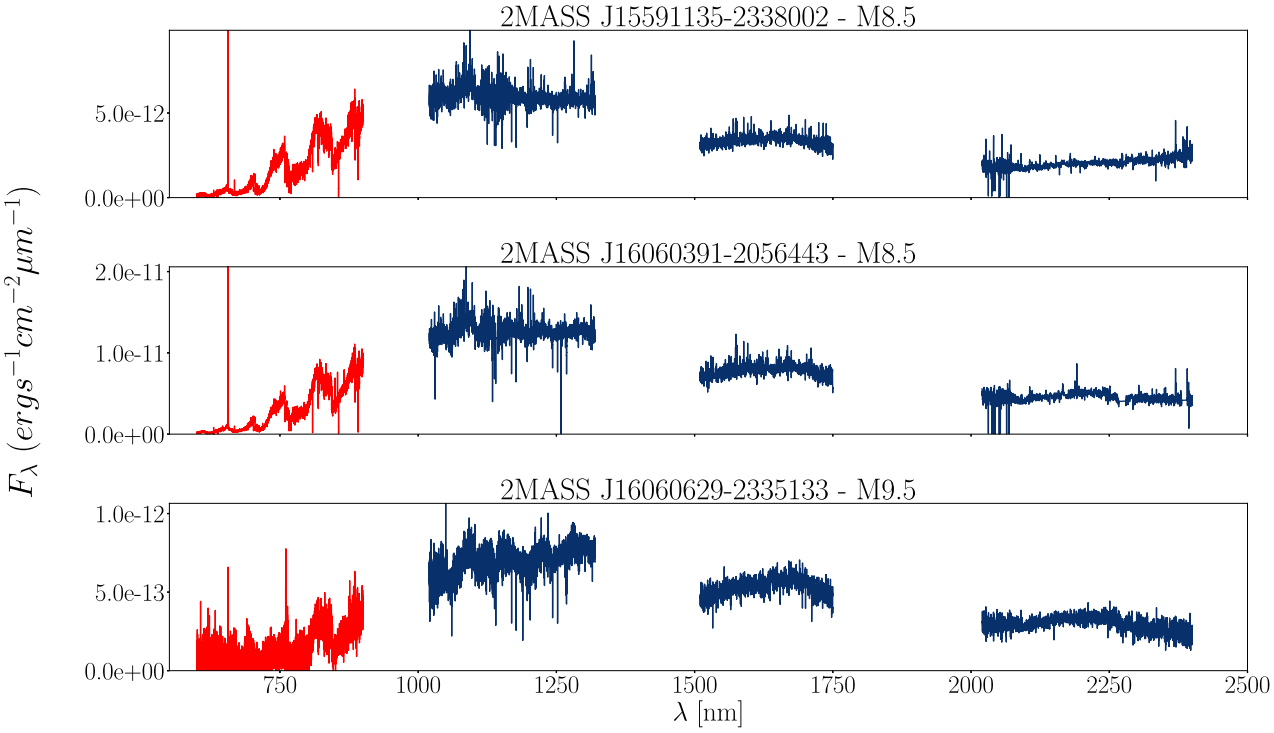

Figure A3. X-shooter/VLT and OSIRIS/GTC spectra for objects from the UppSco association listed in Table 1. The X-shooter optical spectra are shown in red for clarity. The flux density is given in F_λ in erg s^{-1}cm$^{-2}\mu$m^{-1}.

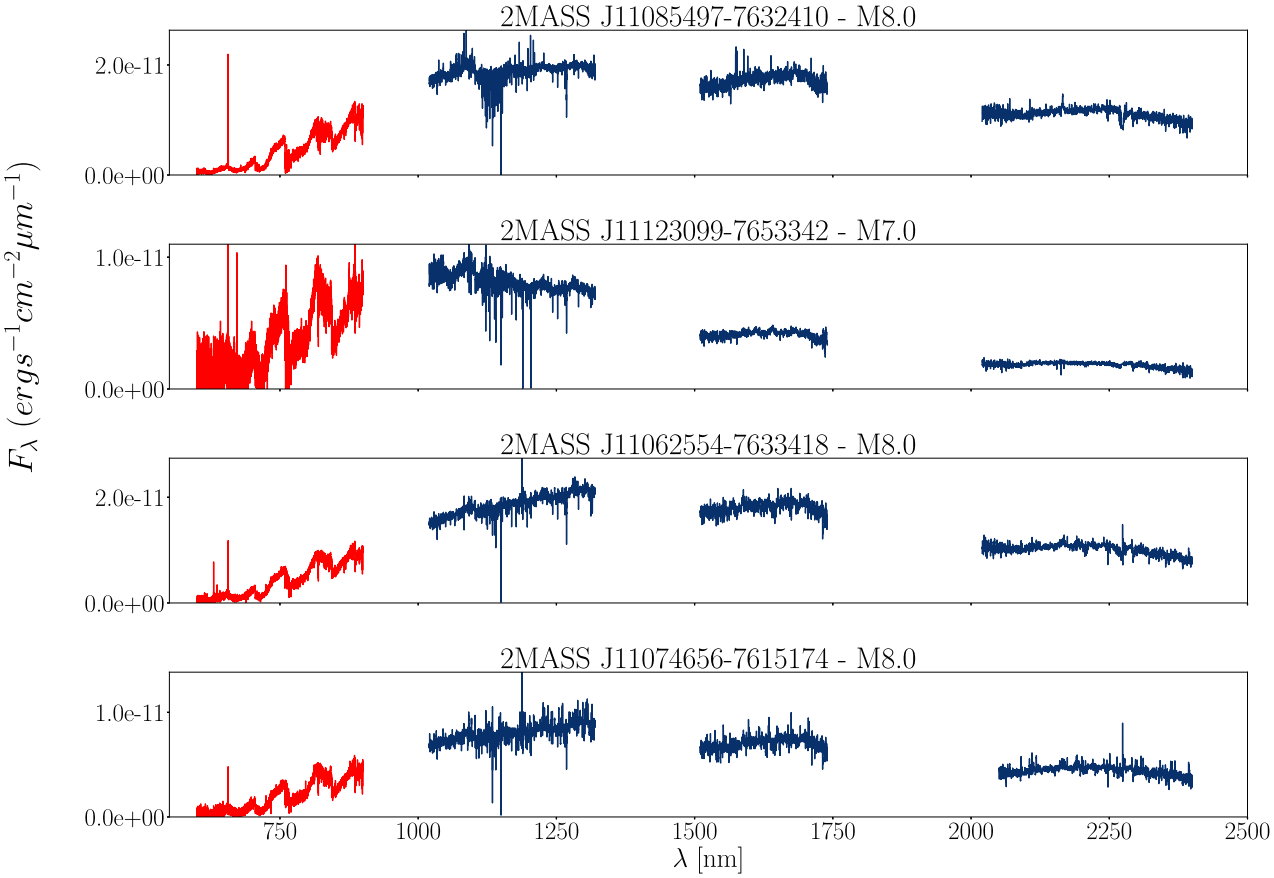

Figure A4. X-shooter/VLT and OSIRIS/GTC spectra for objects from the Cha I association listed in Table 1. The X-shooter optical spectra are shown in red for clarity. The flux density is given in F_λ in erg s^{-1}cm$^{-2}\mu$m^{-1}.

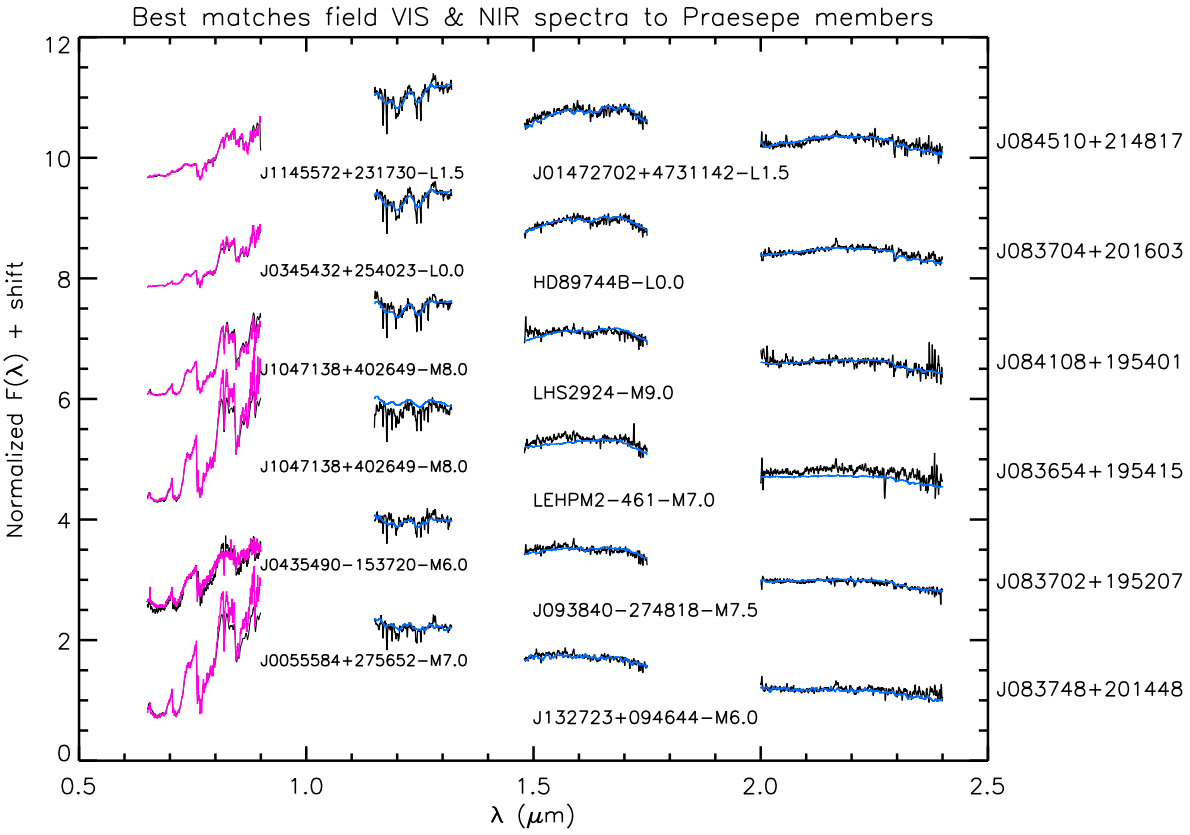

Figure A5. Best field dwarf matches (coloured lines) in the optical and near-infrared for Praesepe members (black).

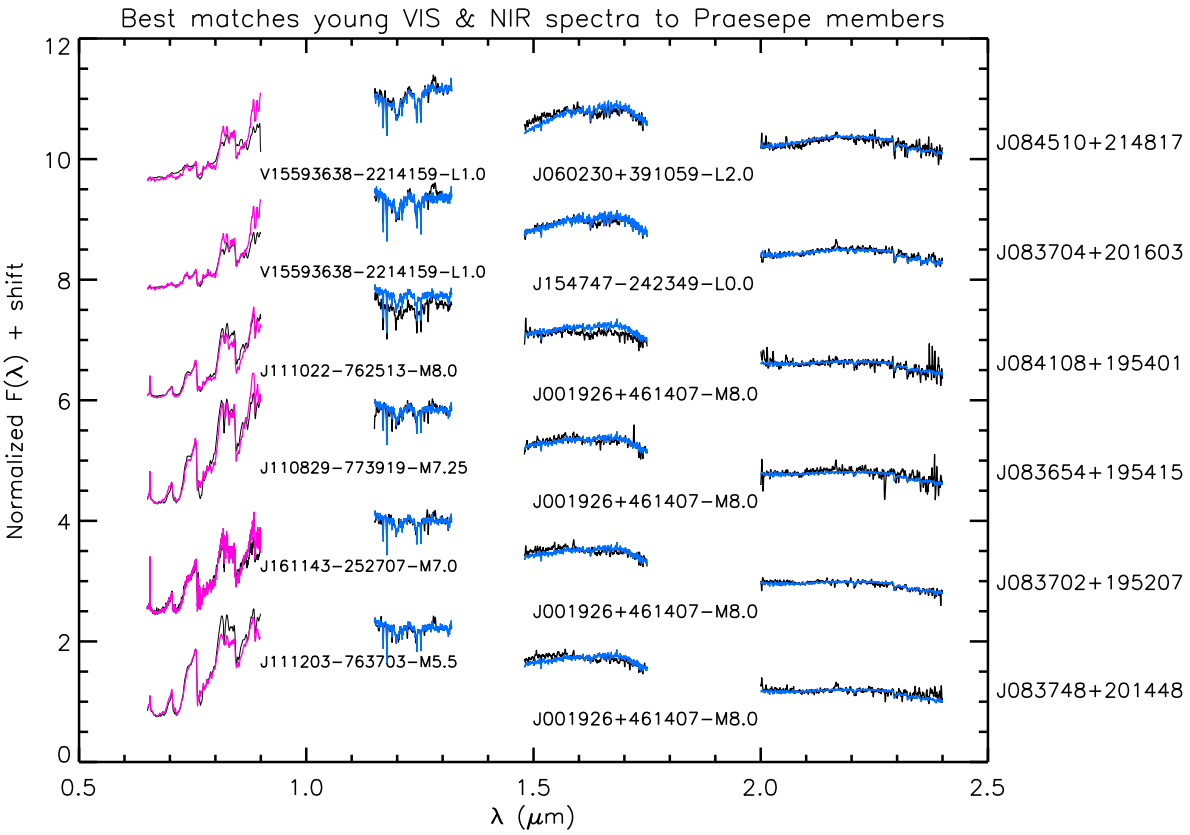

Figure A6. As Fig. A5, but comparing with the library of young M and L dwarfs.

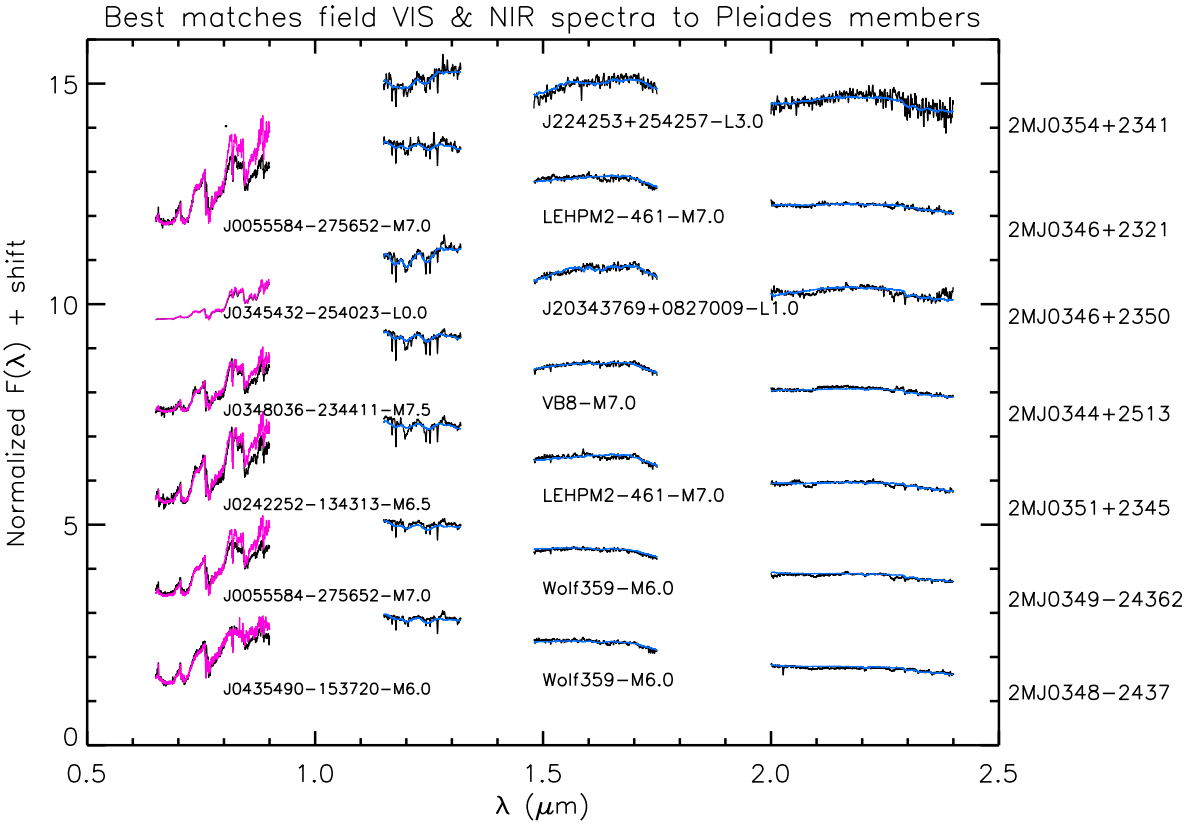

Figure A7. Best field dwarf matches (coloured lines) in the optical and near-infrared for Pleiades members (black).

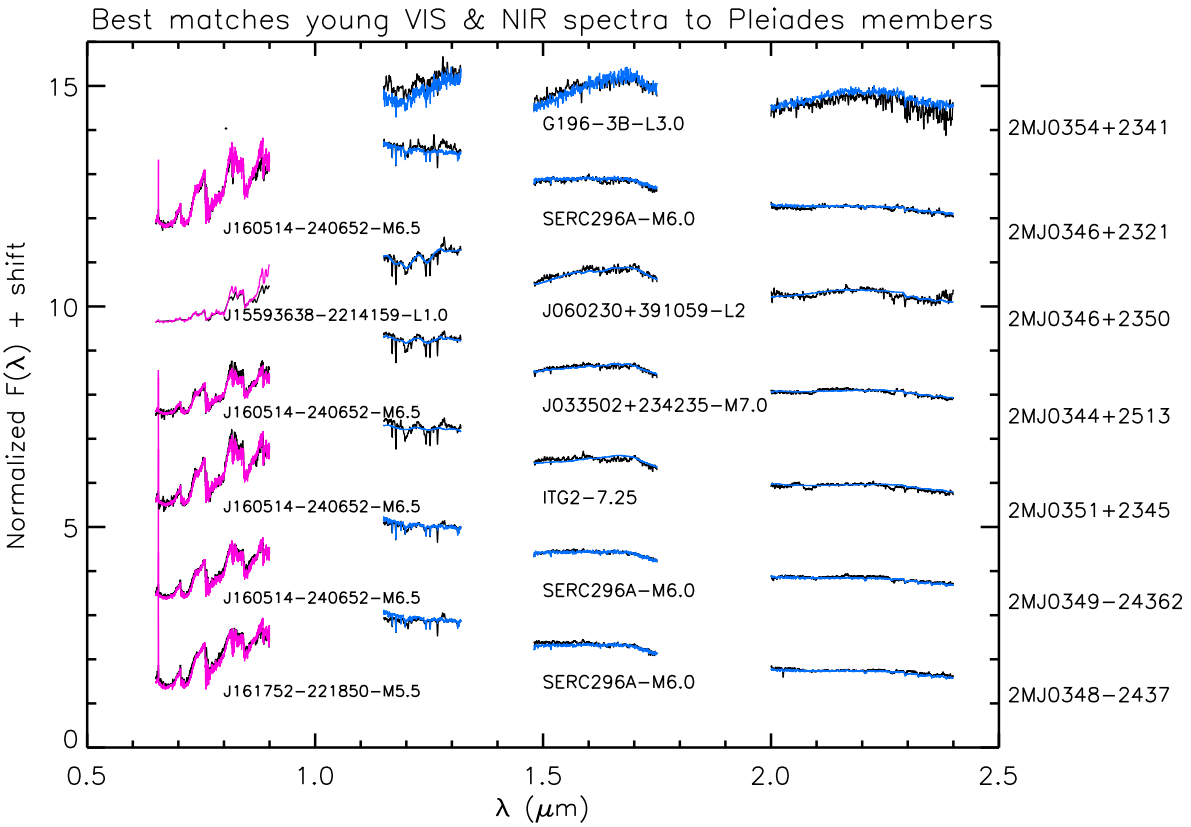

Figure A8. As Fig. A7, but comparing with the library of young M and L dwarfs.

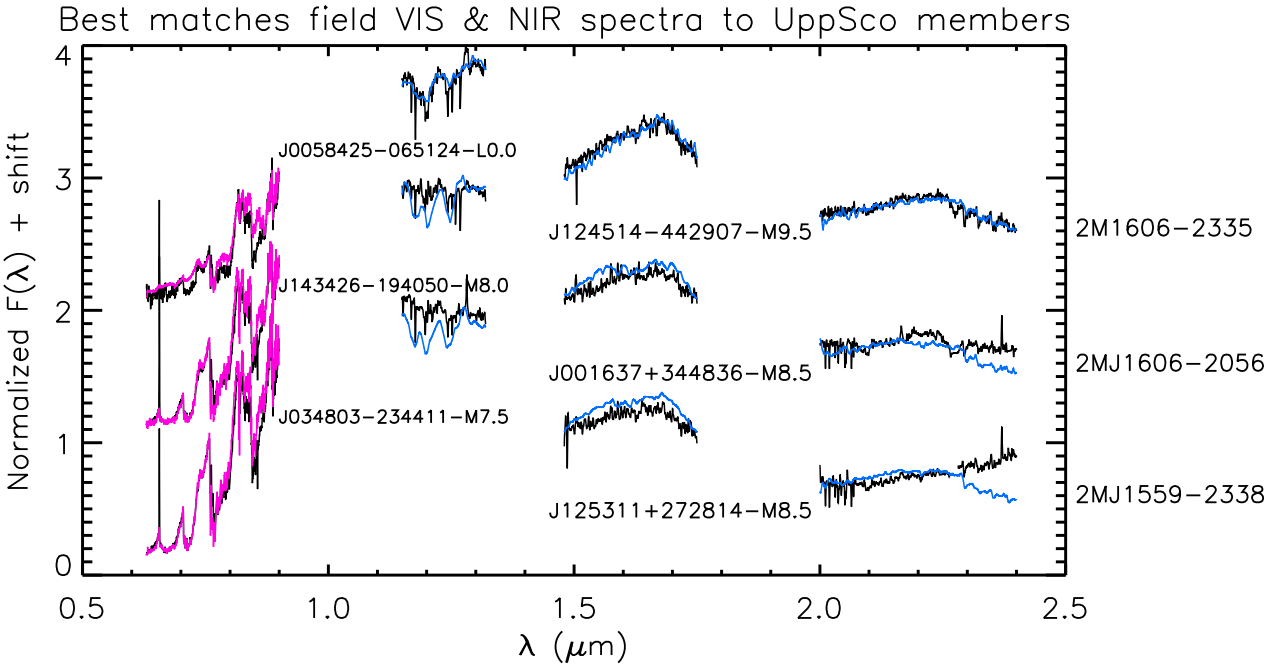

Figure A9. Best field dwarf matches (coloured lines) in the optical and near-infrared for UppSco members (black).

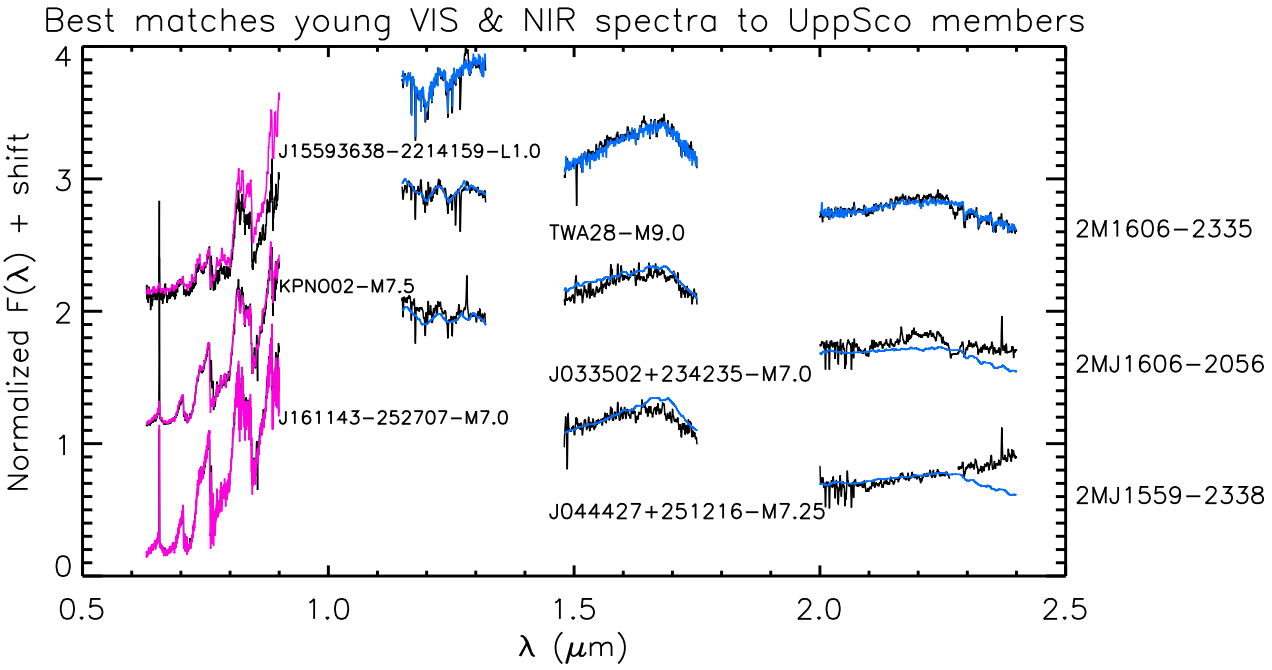

Figure A10. As Fig. A9, but comparing with the library of young M and L dwarfs.

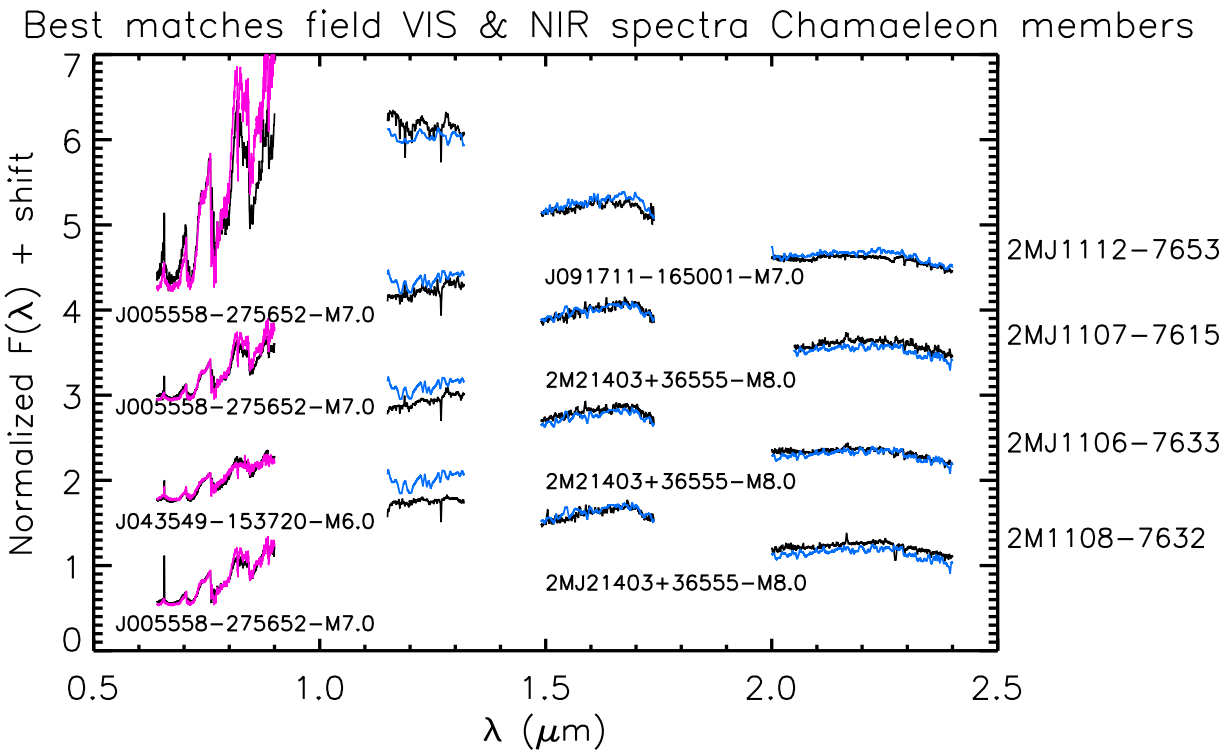

Figure A11. Best field dwarf matches (coloured lines) in the optical and near-infrared for Cha I members (black).

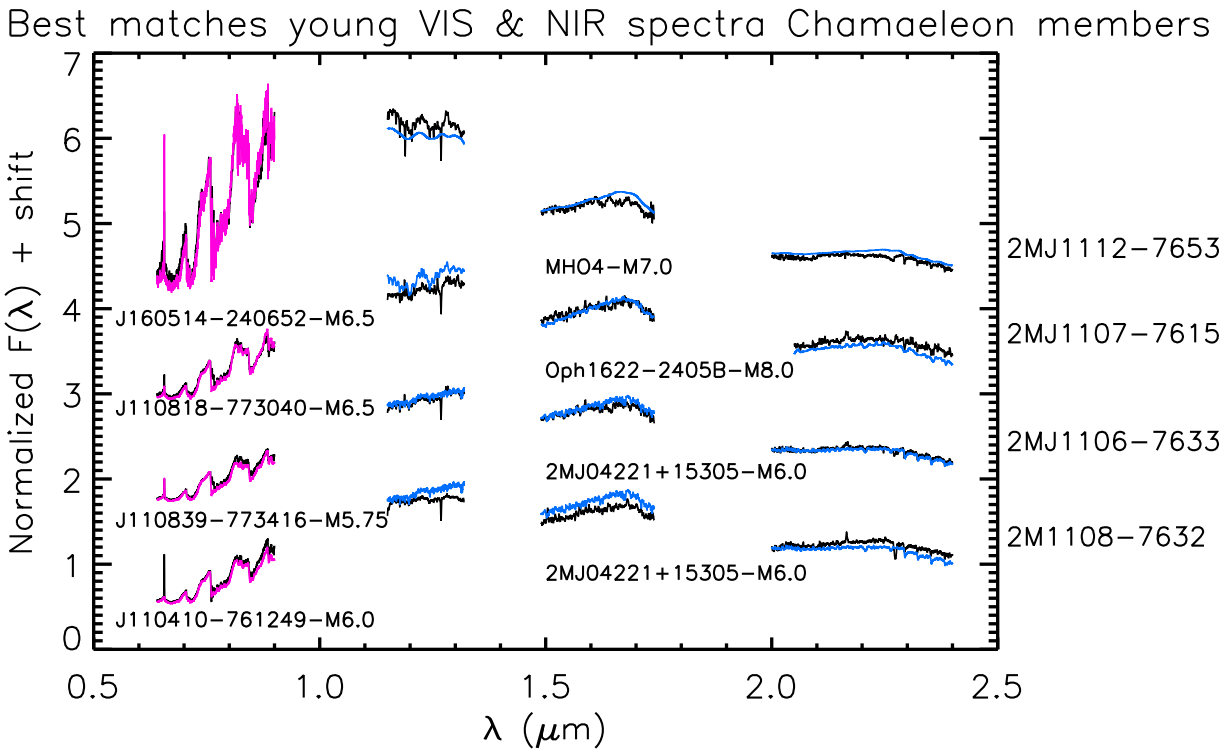

Figure A12. As Fig. A11, but comparing with the library of young M and L dwarfs.

This paper has been typeset from a TEX/LATEX file prepared by the author.